UNIVERSIDADE FEDERAL DO ESPÍRITO SANTO
CENTRO TECNOLÓGICO
PROGRAMA DE PÓS-GRADUAÇÃO EM ENGENHARIA MECÂNICA

BRUNO FURTADO DE MOURA

A NUMERICAL AND STATISTICAL APPROACH TO ESTIMATE STATE VARIABLES IN FLOW-ACCELERATED CORROSION PROBLEMS

VITÓRIA
2014

BRUNO FURTADO DE MOURA

A NUMERICAL AND STATISTICAL APPROACH TO ESTIMATE STATE VARIABLES IN FLOW-ACCELERATED CORROSION PROBLEMS

Dissertation presented to the Graduate Program in Mechanical Engineering of the Federal University of Espírito Santo, as part of the requirements to obtain the title of Master in Mechanical Engineering.

Advisor: Prof. Wellington Betencurte da Silva, D.Sc.

VITÓRIA

2014

BRUNO FURTADO DE MOURA

A NUMERICAL AND STATISTICAL APPROACH TO ESTIMATE STATE VARIABLES IN FLOW-ACCELERATED CORROSION PROBLEMS

Dissertation presented to the Graduate Program in Mechanical Engineering of the Federal University of Espírito Santo, as part of the requirements to obtain the title of Master in Mechanical Engineering.

Approved in August 29th, 2014.

EXAMINING BOARD

Prof. Wellington Betencurte da Silva, D.Sc. - Advisor
Universidade Federal do Espírito Santo (UFES)

Prof. Dr. Marcelo Camargo Severo de Macêdo - Co-Advisor
Universidade Federal do Espírito Santo (UFES)

Prof. Márcio Ferreira Martins, Ph.D.
Universidade Federal do Espírito Santo (UFES)

Prof. Marcelo José Colaço, D.Sc.
Universidade Federal do Rio de Janeiro (UFRJ)

VITÓRIA

2014

Acknowledgements

I would like to thank my professors and friends Márcio, Marcelo, and Wellington for all the support, encouragement, lessons, and discussions during these years. Without them, this work could not have been completed.

To my family and friends for all the support given during hard times.

Abstract

Sequential Monte Carlo (SMC) or particle filter methods have become very popular in the last few years in the statistical and engineering communities. Such methods have been widely used to deal with sequential Bayesian inference problems in several fields. SMC methods are an approximation of sequences of probability distributions of interest, using a large set of random samples, named particles, that are propagated over time with a simple Sampling Importance (SI) distribution as well as resampling techniques as well. In this work we applied Computational Fluid Dynamics (CFD) and two Bayesian filters to a state estimation problem involving the rate of corrosion in a contraction-expansion geometry. The following filters were applied and compared: the Sampling Importance Resampling (SIR) filter and the Auxiliary Sampling Importance Resampling (ASIR) filter. The first model adopted to calculate mass losses does not account for the influence of corrosion products. The second model is based on a double resistance due to the oxygen diffusion toward the wall through the hydrodynamic boundary layer and the oxide layer. Mass loss data over time are obtained from the literature to compare corrosion rates. The main objective of this work is to discuss and compare the performance of the two models in the prediction of corrosion. Also, the influence of the corrosion products on the rate of corrosion is discussed. The best results in corrosion damage estimation were obtained using the ASIR filter.

Keywords: flow-accelerated corrosion, turbulence, CFD, mass transfer, inverse problem, particle filter.

List of Figures

List of Tables

Contents

Chapter 1

Introduction

The corrosion of a material is defined as the deterioration of a material, generally a metallic one, by a chemical or electrochemical reaction. This deterioration can cause undesirable and harmful effects, including the mass loss of the base material.

This phenomenon is, generally, a spontaneous process in which the reaction occurs continuously, transforming the material in such a way that the loss of durability and performance incapacitates the correct application for which it has been designed.

The economic losses due to corrosion are diverse: some are direct, such as the cost of maintenance of protection against corrosion, and some as indirect, such as the replacement of diverse components, loss of the final product, and loss of efficiency of the process.

Flow-accelerated corrosion (FAC) is one of the main factors responsible for failures of components in the industrial environment such as the oil and gas industry. Oil transported from reservoirs to the refineries passes through different processes of separation of impurities such as seawater, a corrosive fluid.

The ability to model the flow and predict the mechanisms of mass loss makes it possible to obtain data related to the equipment. More accurate schedules of maintenance can be defined with those data, allowing unnecessary production stoppages to be avoided. The modeling can also be applied in the stage of design of the component to optimize the geometry.

The objective of the present work is to investigate corrosion models in a complex geometry, specifically, a contraction-expansion geometry. Two different techniques to predict mass loss are

used and compared. The first technique is Computational Fluid Dynamics (CFD) and the second is a new approach in corrosion modeling, the Bayesian filters.

The structure of the dissertation consists of six chapters:

Chapter 1 provides the contextualization of the FAC problematic and its importance in the industrial environment. It also provides information on the goal and structure of the thesis.

Chapter 2 gives an overview of the advances in modeling through numerical simulation of the FAC and also the advances in the inverse problem.

Chapter 3 describes the CFD modeling of the flow. The modeling of mass transfer and corrosion is also shown. Results and verifications are presented at the end of the chapter.

Chapter 4 details the estimation of corrosion through a particle filter and the parameters that influence the mass transfer. Results and verifications are provided as well.

Chapter 5 presents the overall results and a comparison of the approaches to predict the mass loss.

Chapter 6 presents the conclusions and remarks for future works.

Chapter 2

State of Art

FAC is a phenomenon that occurs when the material degrades due to a chemical or electrochemical process that is amplified by the effect of turbulence in the flow. The fluctuations in the liquid water phase bring corrosive species to the metal surface, reacting and forming corrosion products in this region. These fluctuations also remove the corrosion products from the surface, accelerating the corrosion.

A qualitative description of the phenomenon can be seen in Figure 2.1.

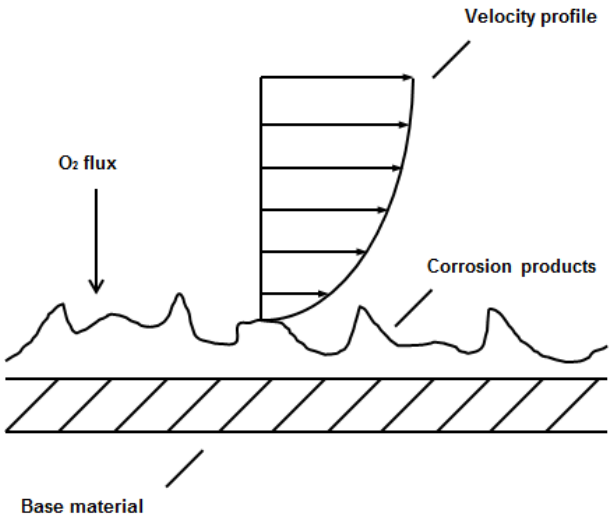

Figure 2.1: Qualitative description of the physical phenomena.

The difficulty in understanding the FAC problem is caused by the motion of the fluid, which causes enhanced rates of corrosion. The intrinsic relationship between the species transport, momentum, and turbulence in the flow makes the roles of all the related physical quantities

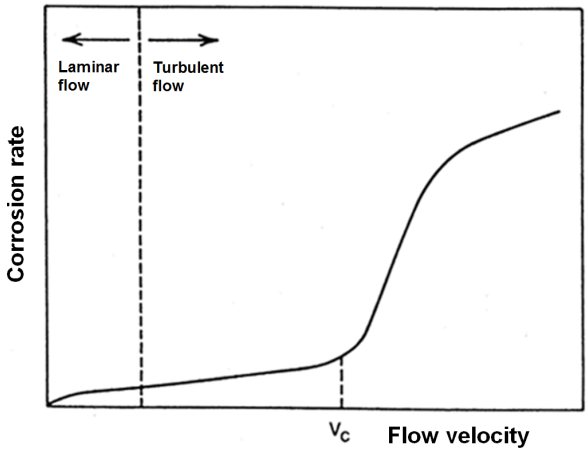

Figure 2.2: Relationship between flow velocity and corrosion rate. (Roberge, 2004)

unclear.

Some physical parameters have been suggested to play a role in FAC rates. Poulson (1993) stated that the hydrodynamic parameters that could control the rates of FAC are the following:

- Velocity
- Surface shear stress
- Intensity of turbulence
- Mass transfer coefficient

The velocity has been widely used as a maximum limit in systems to prevent corrosion damage. A critical velocity that could be considered for severe FAC initiation is indicated. Figure 2.2 shows an example of this practice. Although it may be a common practice, this approach does not give insights into the corrosion process and does not allow the corrosion rates to be calculated.

The surface shear stress, caused by the velocity gradients near the wall, could be the main reason for the enhanced corrosion rates. A critical shear stress could mechanically remove the protective layer of corrosion products from the surface . However it is stated that there is no convincing evidence that this phenomenon occurs in corrosion situations.

The intensity of turbulence could be used as a design parameter. But the use of the turbulence intensity in single-phase flows is more difficult to measure than mass transfer rates. Also, there is no evidence that the correlation with the turbulence intensity is as good as the ones found with mass transfer.

It is widely accepted that many corrosion processes, including that of carbon steel in water, are partially or totally controlled by the mass transfer, in other words, by the transport of the species to the surface. The mass transfer coefficient is defined as the relation between the mass rate of reaction n and the concentration driving force ΔC:

$$K = \frac{n}{\Delta C} \tag{2.1}$$

The mass transfer coefficient is commonly represented as a dimensionless quantity, the Sherwood number, defined as

$$Sh = \frac{Kd}{D} \tag{2.2}$$

where d is the tube diameter and D is the diffusivity of the reactive specie. The Sherwood number is represented generally as a correlation of two different dimensionless numbers, the Reynolds number ($Re = Vd/\nu$, where V is the mean velocity and ν is the kinematic viscosity) and the Schmidt number ($Sc = \nu/D$), of the form:

$$Sh = constant \cdot Re^x Sc^y \tag{2.3}$$

In a subsequent work, Poulson (1999) stated that the various types of flows can be divided into normal flows and separated flows. The differences among these flows can be seen in Table 2.1.

An example of a separated flow is a flow through an orifice. In this type of flow, there is a recirculation region, where the boundary layer detaches and reattaches. These recirculations cause the shear stress to be unrelated to the corrosion rate. The surface shear stress is refuted as a useful parameter to predict corrosion in this type of geometry. Figure 2.3 shows the flow parameters for this geometry downstream of the expansion. The FAC rates may be induced by turbulence eddies or mass transfer in these zones. It is also argued that the turbulent bursting stresses caused by the turbulence flows could physically remove the corrosion products, explaining the same behavior as shown in in figure 2.3 between turbulence and mass loss.

The inherent relation between flow parameters and corrosion and the advances in computational processing capacity have encouraged researchers to model mass loss and flow conditions through CFD.

Nesic and Postlethwaite (1991a) modeled the turbulent flow with a k-ϵ turbulence model by numerical simulation of a single-phase flow to determine the flow structure in a sudden pipe expansion. The results shown that the rates of mass transfer through the boundary layer are

Table 2.1: The two types of flow. (Poulson, 1999)

Normal flow
• Shear stress related to mass transfer • Turbulence created close to wall • If roughness develops it reflects the flow structure • Mass transfer and pressure drop both increase • Corrosion rate increases
Detached flow
• Shear stress and mass transfer not related • Turbulence generated away from the wall • If roughness develops, evidence for increasing mass transfer is less clear • Corrosion rate tends to be constant

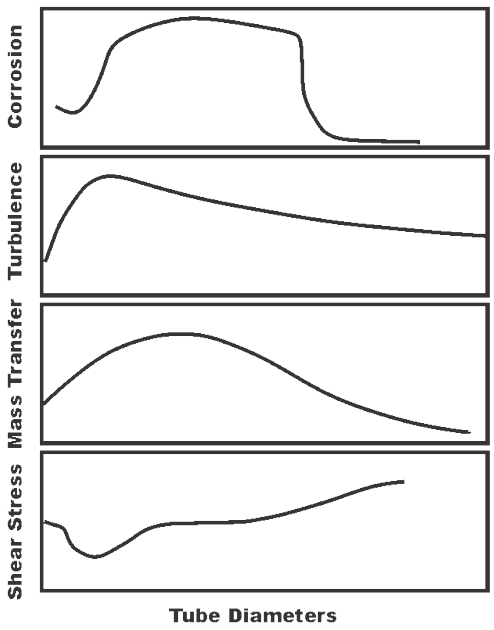

Figure 2.3: Flow parameter and corrosion rates downstream of a flow expansion. (Poulson, 1999)

directly related to the turbulence fluctuations near the wall. Also, in a subsequent work, Nesic and Postlethwaite (1991b) modeled a two-phase flow in which the dominant mode of metal loss is by corrosion in the same geometry.

Furthermore, Nesic et al. (1992) used a low Reynolds number (LRN) k-ϵ turbulence model in a sudden pipe expansion to extend the validity of his work. It was observed that, at high Schmidt numbers, the mass transfer boundary layer is embedded deep within the viscous sublayer, causing the diffusion-controlled mass transfer sublayer to be thinner than the viscous sublayer. Nesic et al. (1993) also showed that the wall function approach would provide poor information on mass transfer near the wall, and thus the LNR treatment would be desirable in that situation.

In the same line, Wang and Postlethwaite (1997) modeled the local mass transfer coefficients with LRN k-ϵ to determine the kinetic diagrams of pipes. Keating and Nesic (1999) used a CFD code to predict hydrodynamic flow fields and mass transfer rates with an LRN k-ϵ for a 180° bend. Davis and Frawley (2008) applied an RNG k-ϵ treatment on the wall in another geometry, a contraction-expansion, and compared the results with experimental data. Understanding that mass transfer is one of the key elements for estimation of the FAC rate, Xiong et al. (2011) modeled the mass transfer by several two-equation eddy-viscosity models and compared the results obtained with a fully developed pipe flow, backward-facing step flow, and an orifice in a pipe flow. Lin and Ferng (2014) investigated the corrosion rate in two different piping systems using CFD in a three-dimensional turbulent single-phase flow model and compared the results with measured data obtained from a pressurized water reactor power plant.

Another use of the CFD codes is the qualitative and curve-fitting methods. Nesic (2006) re-designed the geometry of a bauxite refinery's heat exchanger headers by CFD to decrease the turbulence intensity in the flow to reduce corrosion damage. Figure 2.4 shows the turbulence reduction using a flow correction device to decrease the turbulence.

Ferng et al. (2008) modeled the flow of a boiling water reactor piping system by CFD and used hydrodynamic simulation results such as the lower near-wall fluid velocity and local droplet impingement as an indicator of severe FAC wear. Figure 2.5 shows the plant measured data, predictions of the impingement indicator, and predictions of the low near-wall fluid velocity as a chemical corrosion indicator.

Ferng and Lin (2010) plotted the measured local wall thinning on the wall surface versus the turbulence kinetic energy calculated by a CFD model in order to fit a curve to predict the amount of local wall thinning. The measured data were used in combination with the calculated

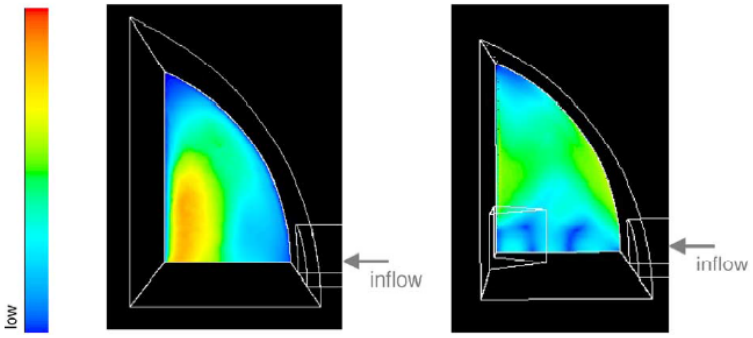

Figure 2.4: Reduction of the turbulent kinetic energy by redesigning the geometry in a bauxite refinery's heat exchanger headers. (Nesic, 2006)

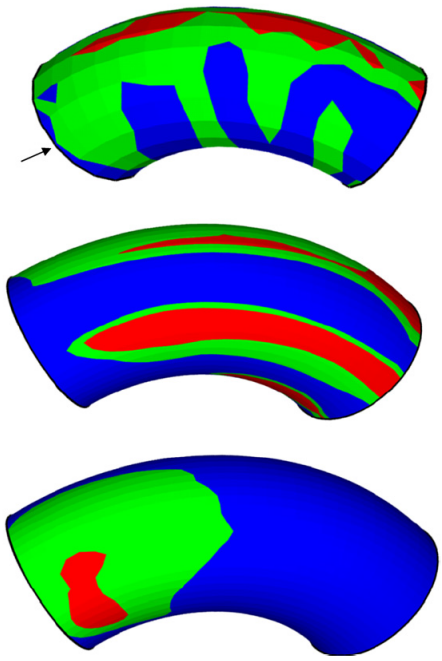

Figure 2.5: Comparison of FAC wear sites for plant measured results, predicted results by droplet impingement indicator, predicted results by chemical corrosion indicator respectively. (Ferng et al., 2008)

hydrodynamic parameter to help the monitoring of the pipe wall.

None of the approaches presented previously model the evolution of the corrosion rates over time, as a steady state condition is assumed to diminish the processing time. Mahato et al. (1968a; 1968b) proposed a model that describes the diffusion of the oxygen under flow conditions through the viscous sublayer and the corrosion products. It was established that the coefficients beta and alpha must be estimated by the measurements obtained from the experiments to fit a curve of the amount of corrosion as a function of the exposure time. Equation 2.4 presents the model.

$$\frac{dW}{dt} = \frac{1}{2\alpha W + \beta} \tag{2.4}$$

$$\alpha = \frac{k}{2D_v C_b} \tag{2.5}$$

$$\beta = \frac{y_1}{C_b(D_v + \epsilon)} \tag{2.6}$$

where W is the mass loss, t is time, k is the resistance coefficient, D_v is the diffusivity of the corrosive species, C_b is the bulk concentration of the corrosive species, y_1 is the fluid viscous sublayer and ϵ is the eddy diffusivity.

To estimate these quantities, an inverse modeling technique can be applied. This technique is based on particle filters to solve a state estimation problem. Such a problem consists in applying the available measurements in combination with prior information about the physical phenomenon with the Bayes' theorem in order to sequentially produce more accurate estimates of the dynamic variables of interest.

The Kalman filter, presented by Kalman (1960), is the most prominent Bayesian filter technique. The drawback of this filter is that it is restricted to linear models and Gaussian processes. To overcome those highly restrictive limitations, particle filters were presented as a solution specifically for non-linear and non-Gaussian processes.

Hammersley and Hanscomb (1964) presented a technique that used recursive Bayesian filters, together with Monte Carlo simulations, known as Sequential Importance Sampling (SIS). The main idea was to describe the Probability Density Functions (PDF) of the state variables as a set of random particles. Each particle was then associated with a weight that was calculated using the measurements along with their uncertainties. The values of the particles and their associated weights allowed a more accurate PDF (posterior) to be retrieved.

To avoid the degeneracy problem, when only a few particles participated effectively in the filtering process, Gordon et al. (1993) added a new step, called resampling, into the SIS filter. Resampling can be applied either if the number of effective particles falls below a specified threshold number or at every step in a technique known as the Sampling Importance Resampling (SIR) filter.

Pitt and Shephard (1999) introduced a new filter, namely the Auxiliary Sampling Importance Resampling (ASIR) filter, which has a new stage of resampling. The main idea was to improve the prior information by using an additional set of particles (called auxiliary particles) so as to reduce the computational cost without degrading the accuracy of the result.

Although estimating the mass transfer coefficient from a corrosion perspective using Bayesian filters is a new investigation, an extensive number of modern studies applied a particle filter in heat transfer estimation. Colaço et al. (2012) compared the performance of the SIR and ASIR filters in the estimation of the heat flux applied to a square cavity in a natural convection problem. The results showed excellent estimates for the time variation of the unknown quantity. Silva (2012) applied the SIR and ASIR filters to a fire propagation problem. Hamilton et al. (2013) applied the SIR filter to estimate the heat transfer coefficient between the product gases and the walls of an internal combustion engine chamber.

Chapter 3

CFD Study of the Hydrodynamic Behavior in Geometries Subject to Flow-Accelerated Corrosion

In this chapter, the turbulence models are implemented in the CFD code ANSYS CFX in a contraction-expansion geometry with single-phase flow to calculate the mass loss caused by mass transfer of oxygen to the reacting surface. Furthermore, the mesh optimization is performed to obtain accurate results. Hydrodynamic properties are investigated as well.

3.1 Conservation Equations

The mathematical description of a fluid flow is based on the conservation equations. These equations are used to calculate the fields of pressure, velocity, and concentration of species in the entire domain. For an incompressible flow and Newtonian fluid, the conservation of mass, momentum, and species equations are respectively:

$$\frac{\partial \rho}{\partial t} + \frac{\partial \left(\rho U_i\right)}{\partial x_i} = 0 \tag{3.1}$$

$$\frac{\partial \left(\rho U_i\right)}{\partial t} + \frac{\partial \left(\rho U_i U_j\right)}{\partial x_j} = \frac{\partial}{\partial x_j}\left(\mu \frac{\partial U_i}{\partial x_j}\right) - \frac{\partial p}{\partial x_i} + \rho g_i \tag{3.2}$$

$$\frac{\partial(\rho C)}{\partial t} + \frac{\partial(\rho U_j C)}{\partial x_j} = \frac{\partial}{\partial x_j}\left[D\frac{\partial(\rho C)}{\partial x_j}\right] \tag{3.3}$$

where U is the velocity, C is the concentration of oxygen, p is the pressure, x is the axial coordinate, t is the time, ρ is the fluid density, μ is the dynamic viscosity, D is the diffusivity and g is the gravity.

The modeling of fluid dynamics was performed using CFD. The code used for this modeling was ANSYS CFX. The finite volume method was used. The equations are applied in discrete domains in a fixed area of space known as volume control that approximates the discretized equations to the differential form (Versteeg and Malalasekera, 2007; Patankar, 1980).

3.2 Turbulence Model

Turbulence is a phenomenon in which the flow becomes chaotic, random, and also transient even if the boundaries conditions imposed are steady. The velocity and all other fluid properties vary randomly and chaotically over time. The behavior of the velocity in a fixed position is shown in Figure 3.1.

Due to the complexities of the nature of the flow, the properties are decomposed into a steady mean value, $\overline{\phi}$, on which a fluctuation value, ϕ', is superimposed, and replaced in Equations 3.2, 3.3. Substitution of those terms gives the time-average momentum and time-average transport of the species equation.

$$\frac{\partial\left(\rho\overline{U_i}\right)}{\partial t} + \frac{\partial\left(\rho\overline{U_i U_j}\right)}{\partial x_j} = \frac{\partial}{\partial x_j}\left[-p\delta_{ij} + \mu\left(\frac{\partial\overline{U_i}}{\partial x_j} + \frac{\partial\overline{U_j}}{\partial x_i}\right) - \rho\overline{u_i' u_j'}\right] + \rho g_i \tag{3.4}$$

$$\frac{\partial\left(\rho\overline{C}\right)}{\partial t} + \frac{\partial\left(\rho\overline{U_j C}\right)}{\partial x_j} = \frac{\partial}{\partial x_j}\left[D\frac{\partial\left(\rho\overline{C}\right)}{\partial x_j} - \rho\overline{u_j' c'}\right] \tag{3.5}$$

The turbulence models allow the calculation of the new terms introduced when the time-average equations for the momentum and species equation are solved. These terms are the Reynolds stresses, $-\rho\overline{u_i' u_j'}$, and the turbulent diffusion fluxes, $-\rho\overline{u_j' c'}$.

The eddy viscosity models are based on the presumption that an analogy exists between the viscous stresses and the Reynolds stresses on the mean flow. The viscous stresses are taken to

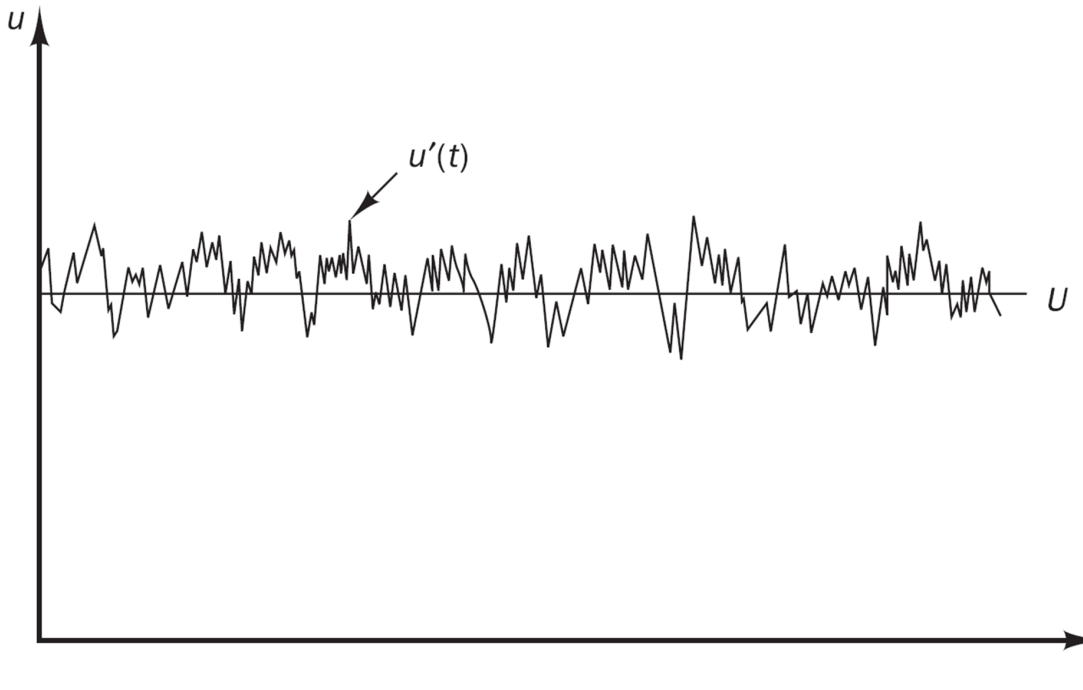

Figure 3.1: Velocity measurement in a turbulent flow over time at a point. (Versteeg and Malalasekera, 2007)

be proportional to the rate of deformation. Thus, the Boussinesq hypothesis gives

$$\tau_{ij} = -\rho\overline{u_i' u_j'} = 2\mu_t S_{ij} \tag{3.6}$$

where μ_t is the eddy viscosity and S_{ij} is the mean strain-rate tensor defined as

$$S_{ij} = \frac{1}{2}\left(\frac{\partial\overline{U_i}}{\partial x_j} + \frac{\partial\overline{U_j}}{\partial x_i}\right) \tag{3.7}$$

By analogy, the turbulent transport of species is

$$-\rho\overline{u_j' c'} = D_t\left[\frac{\partial\overline{C}}{\partial x_j}\right] \tag{3.8}$$

where D_t is the eddy diffusivity.

Since the mechanism of turbulent transport of momentum and mass is the same, eddy mixing, it is expected that values of eddy diffusivity will be close to the turbulent viscosity. Thus, the turbulent Schmidt number is defined as:

$$Sc_t = \frac{\mu_t}{\rho D_t} \tag{3.9}$$

Most CFD codes use a value near to 1 for the turbulent Schmidt number.

The k - ϵ turbulence model proposed by Launder and Spalding (1972), a consolidated model that is widely used in various applications, is a two-equation eddy viscosity model. The equations that represent the effects of turbulence in the flow are the turbulent kinetic energy, k , and the turbulent dissipation rate, ϵ. However, the k - ϵ turbulence model fails to compute flows with strong adverse pressure gradients and separation.

In the regions near the wall, the k - ω turbulence model proposed by Wilcox (1988) is substantially more accurate. The equations that represent the effects of turbulence in the flow are the turbulent kinetic energy, k and specific dissipation rate, ω. The downside of this model is that it fails in the freestream outside the boundary layer.

The Shear Stress Transport (SST) k - ω proposed by Menter (1994) is a model based on a blending function which ensures a proper selection of the k - ϵ in freestream and k - ω in the near wall. The equations' formulations are given as:

$$\frac{\partial\left(\rho k\right)}{dt}+\frac{\partial\left(\rho\overline{U_i}k\right)}{\partial x_i}=\tilde{P}_k-\beta^*\rho k\omega+\frac{\partial}{\partial x_i}\left[\left(\mu+\sigma_k\mu_t\right)\frac{\partial k}{\partial x_i}\right] \tag{3.10}$$

$$\frac{\partial\left(\rho\omega\right)}{dt}+\frac{\partial\left(\rho\overline{U_i}\omega\right)}{\partial x_i}=\alpha_t\rho S^2-\beta_t\rho\omega^2+\frac{\partial}{\partial x_i}\left[\left(\mu+\sigma_\omega\mu_t\right)\frac{\partial\omega}{\partial x_i}\right]+2\left(1-F_1\right)\rho\sigma_{w2}\frac{1}{\omega}\frac{\partial k}{\partial x_i}\frac{\partial\omega}{\partial x_i} \tag{3.11}$$

where F_1 is the blending function, which is equal to zero in the region away from the surface (k - ϵ turbulence model)and switches to one in the region inside the boundary layer (k - ω turbulence model). A limiter is used for the production term in order to prevent the build-up of turbulence in stagnation regions:

$$\tilde{P_k}=min(P_k,10\cdot\beta^*\rho k\omega),\qquad P_k=\mu_tS^2,\qquad S=\sqrt{2S_{ij}S_{ij}} \tag{3.12}$$

The eddy viscosity is defined as:

$$\mu_t=\frac{\rho a_1k}{max(a_1\omega,SF_2)} \tag{3.13}$$

where F_2 is a second blending function.

The constants are computed by linear combination of the corresponding constants of k - ϵ and k - ω models through $\Phi_3=F_1\Phi_1+(1-F_1)\Phi_2$. The constants for this model are: $\beta^*=0.09$, $\alpha_{t1}=5/9$, $\beta_{t1}=3/40$, $\sigma_{k1}=0.85$, $\sigma_{\omega1}=0.5$, $\alpha_{t2}=0.44$, $\beta_{t2}=0.0828$, $\sigma_{k2}=1$, and $\sigma_{\omega2}=0.856$.

3.3 Wall Treatment

Due to the presence of a solid boundary condition, the boundary layer on a flat plate is essentially different from a flow under free stream conditions due to the no-slip condition.

There will be a substantial region of the flow away from the wall dominated by inertial forces, a region where inertial and viscous forces are of similar magnitude and a region where there is a thin layer of viscous effects. Near the wall, the flow is influenced by viscous effects and does not depend on the freestream properties. The mean flow velocity only depends on the distance from the wall y, fluid density ρ, dynamic viscosity μ and wall shear stress τ_w.

Therefore, a dimensional analysis gives the law of the wall that contains the definition of the dimensionless velocity u^+ and dimensionless wall distance y^+:

$$u^+ = \frac{U}{u_\tau} = f\left(\frac{\rho u_\tau y}{\mu}\right) = f\left(y_+\right) \tag{3.14}$$

where the friction velocity is defined as

$$u_\tau = \sqrt{\frac{\tau_w}{\rho}} \tag{3.15}$$

The viscous sublayer is in practice very thin ($y^+ < 5$) and the following relationship is valid:

$$u^+ = y^+ \tag{3.16}$$

Outside the viscous sublayer ($30 < y^+ < 500$) there is a region in which the viscous and inertial forces are both important. In this region, the log-law layer is

$$u^+ = \frac{1}{\kappa} ln\left(y^+\right) + B \tag{3.17}$$

where κ is the von Kármán constant and B = 5.5 for smooth walls.

ANSYS CFX software uses two distinct models for the wall treatment. The wall function model uses empirical formulas that impose appropriate conditions near the wall, without fully resolving the boundary layer, thus saving computational resources. The LRN turbulence model solves the details of the viscous sublayer and the diffusion-controlled concentration boundary layer, improving the accuracy near the wall. In the case of turbulence models based on the k - ϵ model, the wall function method is implemented, so the resolution of the boundary layer is limited. The turbulence models based on the ω equation, such as SST k - ω, are more suitable for implementing the LRN turbulence model.

3.4 Corrosion Model

Keating and Nesic (1999) formulated a model from an example of corrosion under diffusional control of oxygen.

$$\begin{aligned} &2Fe \rightarrow 2Fe^{++} + 4e^{-} \\ &O_2 + 2H_2O + 4e^{-} \rightarrow 4OH^{-} \end{aligned} \tag{3.18}$$

The flux of species, n, is determined:

$$n = k_m(C_b - C_w) \tag{3.19}$$

where C_b is the bulk concentration of oxygen and C_w is the concentration of oxygen on the wall. It is assumed that all of the wall concentration is immediately consumed by the corrosion reaction, so $C_w = 0$. According to Equation 3.18, two moles of Fe react with each mole of O_2.

So the corrosion rate can be determined:

$$\frac{dW}{dt} = 2k_m C_b \tag{3.20}$$

where W is the mass loss of Fe.

In a fully developed fluid flow with simple geometry, the mass transfer coefficient can be calculated by an empirical correlation (Berger and Hau, 1977). But for flow with a sudden change the unique possibility is calculated through the concentration field already solved by the mass transfer coefficient definition.

$$k_m = -D\frac{\partial C_0/\partial y|_{y=0}}{C_b} = -\frac{D}{\Delta y}\frac{C_0}{C_b} \tag{3.21}$$

3.5 Characterization of the Problem

In order to validate the numerical formulation, the experimental data of Lotz and Postlethwaite (1990) were obtained for comparison. A saline solution was pumped through a nozzle with a contraction-expansion made of carbon steel. The solution domain was a contraction-expansion with an aspect ratio of 1.8:1:2. A schematic is shown in Figure 3.2. The dimensions of the computational domain are given in Table 3.1.

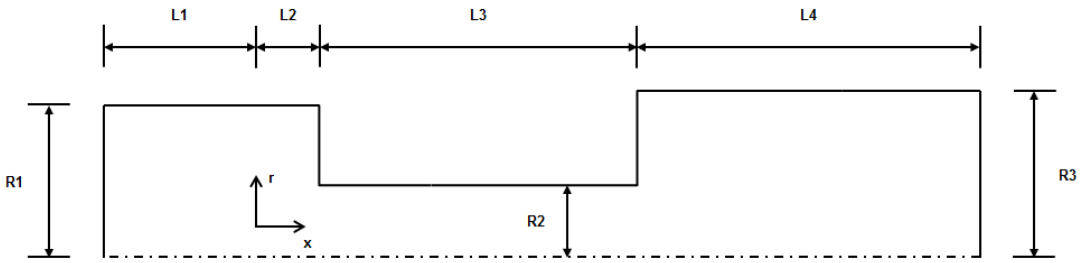

Figure 3.2: Schematic of the computational domain.

Table 3.1: Dimensions of the computational domain.

Length (mm)		Radius (mm)	
L1	256.8	R1	19.3
L2	21.2	R2	10.5
L3	222	R3	21
L4	840		

3.5.1 Boundary Condition

In the computational modeling, it was assumed that the flow is an incompressible, isothermal, turbulent flow of saline water in a contraction-expansion . Since there is no swirl component in the flow, the modeling was done in a two-dimensional axisymmetric pipe. This configuration allows the computational effort to be decreased. The Schmidt number is 369 and the salt water saturated with oxygen has a concentration of 6.23 mg L^{-1} (Lewis, 2006).

The inlet conditions are the same as those used by Davis and Frawley (2008). For a turbulent fully developed velocity, the following relation is valid:

$$u_x = u_p \left(1 - \frac{r}{R}\right)^{\frac{1}{7}} \tag{3.22}$$

where r is the radius distance from the center line and R is the radius in the inlet. Integrating Equation 3.22, a relation between the peak velocity and bulk velocity is obtained.

$$u_p = 1.224 u_b \tag{3.23}$$

A value of 3.9 m s^{-1} is set for the bulk velocity.

A linear relationship between near-wall turbulence kinetic energy, k_{nw}, and bulk turbulence kinetic energy, k_b, is assumed for the turbulent kinetic energy inlet boundary condition, k:

$$k = k_b + \frac{r}{R}\left(k_{nw} - k_b\right) \tag{3.24}$$

The near-wall turbulent kinetic energy is given by

$$k_{nw} = \frac{u_\tau^2}{\sqrt{C_\mu}} \tag{3.25}$$

where the friction velocity, u_τ, is defined in Equation 3.15 and C_μ is a constant of the turbulence model. The wall shear stress is

$$\tau_w = \frac{f \rho u_b^2}{2} \tag{3.26}$$

The friction factor, f, using the Blasius equation (White, 1991) is valid for Reynolds numbers between 4×10^3 and 10^5:

$$f = 0.079 \left(\frac{\rho u_b d}{\mu} \right)^{-0.25} \tag{3.27}$$

The turbulent kinetic energy from the center line is

$$k_b = \frac{3}{2} I^2 u_b^2 \tag{3.28}$$

where the turbulent intensity, I, is set as 0.037.

The inlet boundary condition of the specific dissipation rate is

$$\omega = \frac{k^{1/2}}{C_\mu l} \tag{3.29}$$

where l is the turbulence length scale, a physical quantity related to the eddies in the flow. In a fully developed flow, the turbulent length scale is related to the diameter, d, by

$$l = 0.07d \tag{3.30}$$

In the outlet, for mass and momentum, CFX varies the pressure, according to the downstream conditions of the flow, from a pressure value imposed previously. For the turbulence properties, CFX imposes a constant gradient constraint as the boundary conditions.

For the symmetry, the properties normal to the boundary are set to zero:

$$\frac{\partial \bar{\phi}}{\partial y_n} = 0 \tag{3.31}$$

In the wall, both velocity and concentration are zero.

3.5.2 Mesh Structure

The mesh was made with a high density of nodes near the wall, so it could reach an appropriate y^+ value and fully resolve the concentration boundary layer (Nesic et al., 1992, 1993). The software used to construct the mesh was ANSYS ICEM. The mesh can be seen in Figure 3.3.

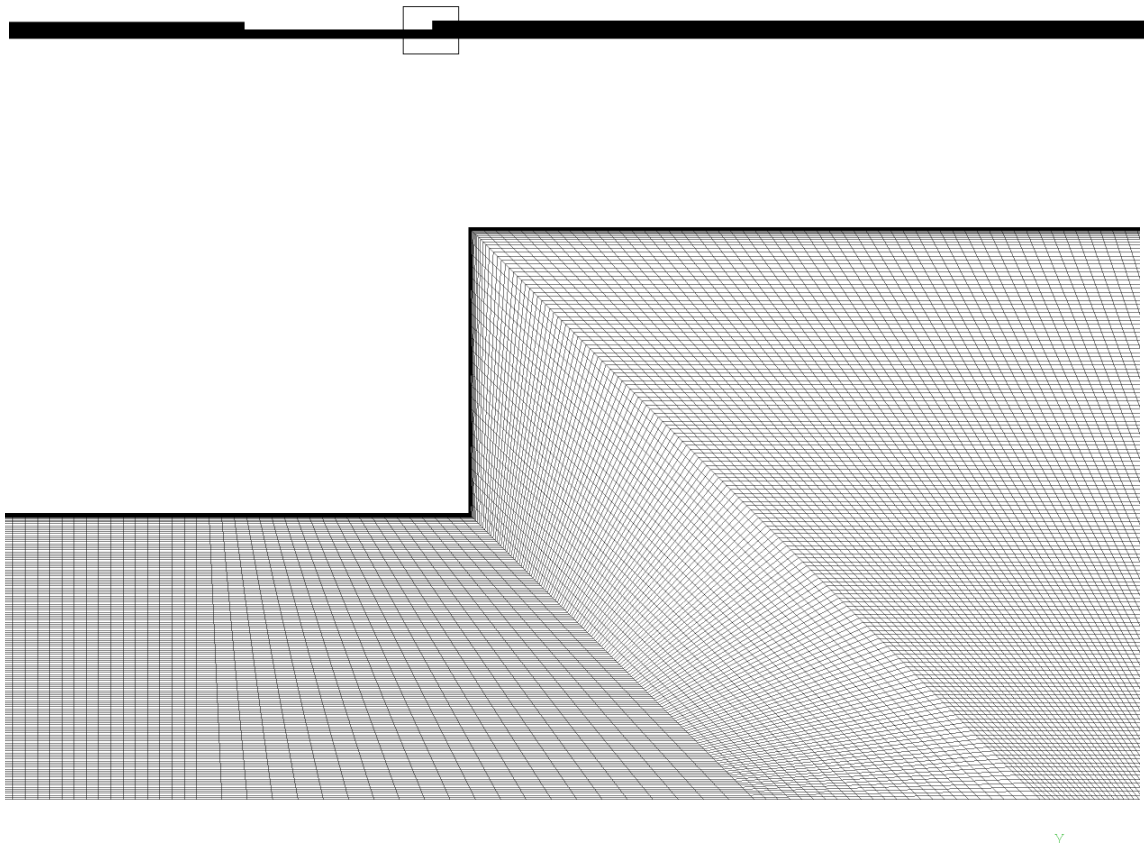

Figure 3.3: Mesh grid utilized to solve the transport equations.

3.6 Results and Discussion

To investigate whether the mesh interferes with the results, the influence of the grid is analyzed. The conducted simulations tested four different mesh node densities in the near-wall region. The information about the meshes can be seen in Table 3.2.

Table 3.2: Number of nodes and elements of the meshes.

Mesh	Number of Nodes	Number of Elements
1	1 066 680	530 198
2	1 295 420	644 112
3	1 418 000	705 256
4	2 127 000	1 059 656

The results in Figure 3.4 show convergence for the mass transfer coefficient and the turbulence kinetic energy. The large discrepancies of the velocity in mesh 1 indicate that the velocity boundary layer is not properly solved.

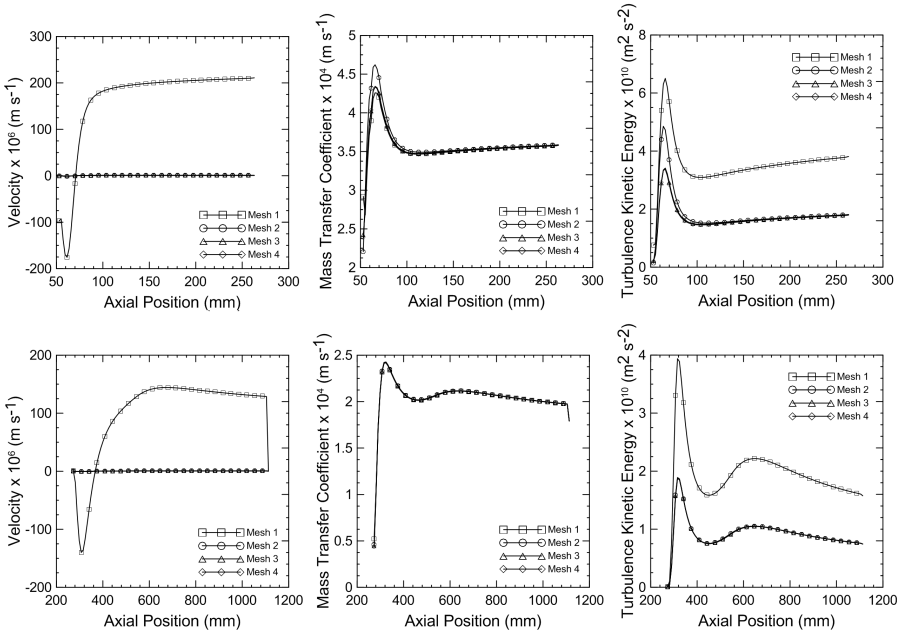

Figure 3.4: Near-wall velocity, mass transfer and turbulence along the contraction and the expansion for different meshes.

The streamlines in Figure 3.5 caused by the sudden change in geometry show the recirculation in the contraction and the expansion. In those regions, the boundary layer detaches, creating a backward flow. Figure 3.6 shows that the regions of separation of the flow are directly related to

the increase of mass transfer and turbulence kinetic energy.

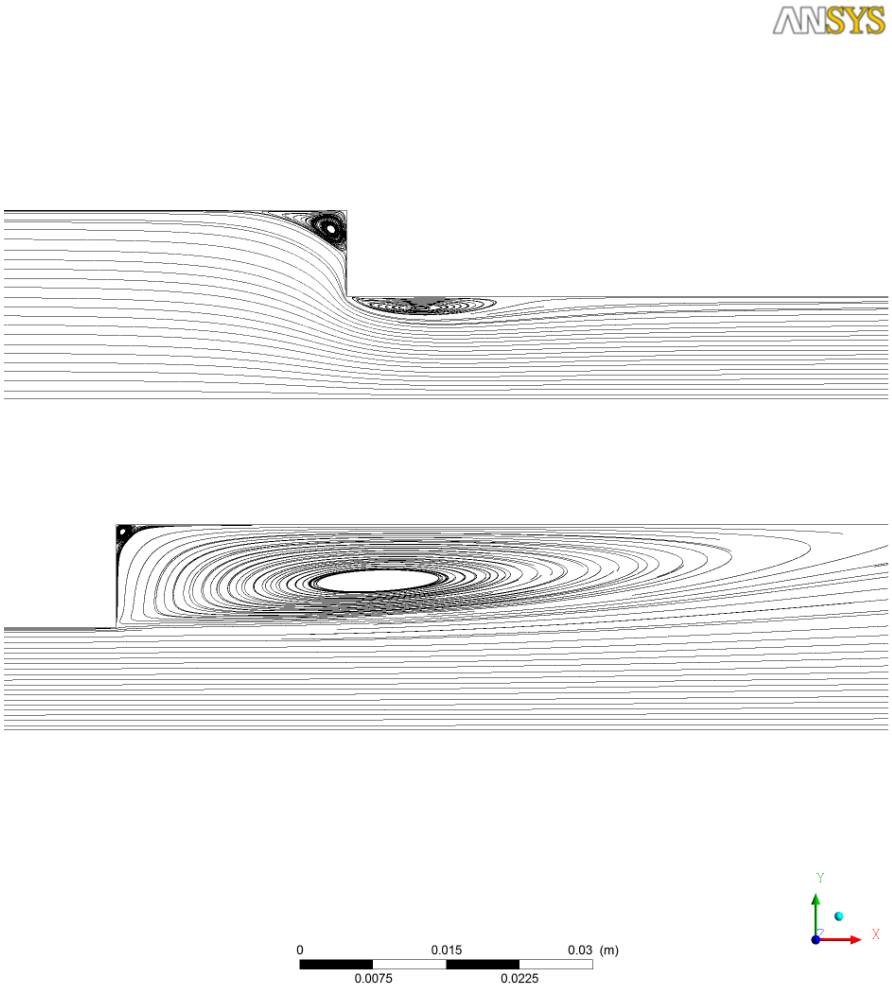

Figure 3.5: Recirculations in the contraction and expansion respectively.

The effective diffusivity and velocity boundary layer are analyzed in Figure 3.7. The effective thickness through which oxygen diffuses is approximately 2 mm upstream of the contraction (the viscous sublayer thickness), 1 mm in the contraction recirculation, and approximately 4 mm in the recirculation located in the expansion. The effective diffusion is 4.19×10^{-5}, 4.09×10^{-5}, 1.54×10^{-5} m^2 s^{-1} respectively upstream of the contraction, 1.34×10^{-5} m^2 s^{-1} in the contraction and 4.74×10^{-5} m^2 s^{-1} in the expansion.

To validate the corrosion model, the rates of mass loss are calculated for each sector of the geometry and compared with experimental data of Lotz and Postlethwaite (1990). Figure 3.8 presents the results calculated by Equation 3.20.

The values of mass loss rate are overestimated in all regions of the domain. The deviations can be explained by one main cause. In the wall region, metal is under the corrosion process and corrosion products precipitate in the wall. Those products works as a resistance to mass transfer

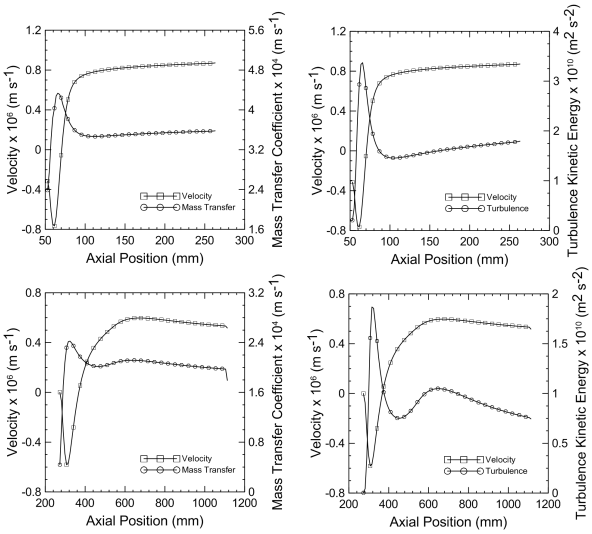

Figure 3.6: Near-wall velocity compared with turbulence and mass transfer along the contraction and expansion region.

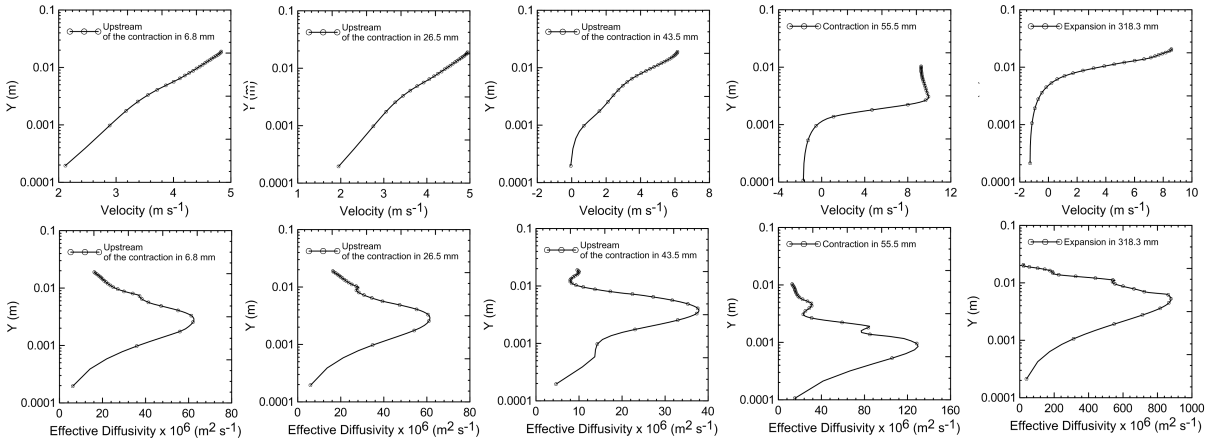

Figure 3.7: Effective diffusivity and velocity boundary layer in the recirculation zone.

of oxygen to the metal surface. The influence of corrosion products is neglected in the model, greatly increasing the mass transfer of oxygen to the surface and, consequently, the mass loss.

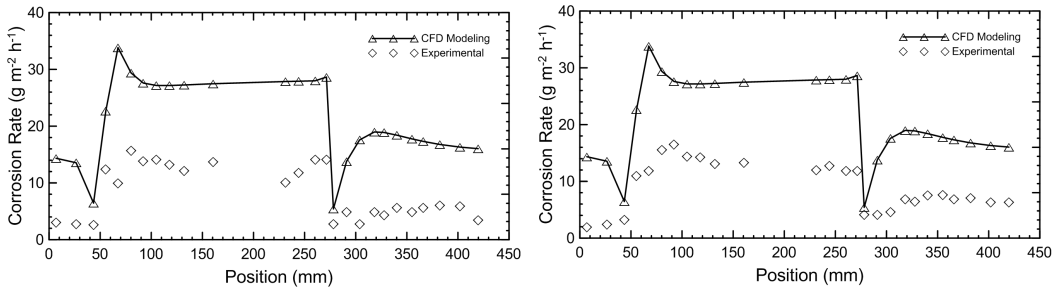

Figure 3.8: Mass loss rate compared with experimental data of Lotz and Postlethwaite (1990) in 25 and 48 h.

To further improve the results, it is imperative to consider both the viscous boundary layer and the corrosion products precipitated in the wall as resistance to the diffusion of oxygen to the surface of the base material. The modeling of those resistances would cause a decrease in the rates of mass loss of the base material, considerably improving the accuracy of the results.

Chapter 4

A Comparison of Two Bayesian Filters Applied in a Flow Accelerated Corrosion Problem

The previous chapter stated the importance of the modeling of the corrosion products. In this chapter, a new model is applied to predict the mass losses of the base material. Due to the unknown nature of the resistance coefficient presented in the model, an inverse problem technique is implemented in this case. The SIR and ASIR particle filter algorithms are implemented in a contraction-expansion geometry with single-phase flow to estimate the mass loss caused by mass transfer of oxygen to the reacting surface. Furthermore, the accuracies of the results of those filters are compared.

4.1 Inverse Problem

The solution of the inverse problem through the Bayesian method aims to statistically infer the posterior probability density. This is accomplished through the Bayes' theorem. It combines the new information (measurements) with previously available (prior) information (prior). The Bayes' theorem is stated as (Kaipio and Somersalo, 2004):

$$\pi_{posterior}\left(P\right) = \pi\left(P|Z\right) = \frac{\pi\left(Z|P\right)\pi\left(P\right)}{\pi\left(Z\right)} \tag{4.1}$$

where P is the parameter analyzed, Z is the measurements, $\pi_{posterior}\,(P)$ is the posterior probability density, $\pi\,(P)$ is the prior density, $\pi\,(Z|P)$ is the likelihood function and $\pi\,(Z)$ is the marginal probability density of the measurements, which plays the role of a normalizing constant.

By assuming that the measurement errors are Gaussian random variables with zero means and that the measurement errors are additive and independent of the parameters x_k, the likelihood function can be expressed as (Kaipio and Somersalo, 2004)

$$\pi(Z|P) = (2\pi)^{-U/2}\,|M_{cov}|^{-1/2}\,exp\left[-\frac{1}{2}\,(Z - W\,(x))^T\,M_{cov}^{-1}\,(Z - W\,(x))\right] \tag{4.2}$$

where M_{cov} is the covariance matrix of the errors.

4.1.1 Sensitivity Coefficient

The sensitivity coefficient plays an important role in state estimation problems (Ozisik and Orlande, 2000). It is defined as

$$J_{ij}\,(P) = \frac{\partial W_i}{\partial P_j} \tag{4.3}$$

where i is the total number of measurements and j is the total number of unknown state variables.

A small value of the magnitude of J_{ij} indicates that large changes in P_j yields small changes in W_i and becomes a very difficult task to estimate the state variable, because basically the same value for mass loss would be obtained for a wide range of values of P_j. Implementation of an iterative procedure for the sensitivity coefficients requires the matrix $J^T J$ to be nonsingular or

$$\left|J^T J\right| \neq 0 \tag{4.4}$$

where $|.|$ is the determinant.

4.1.2 State Estimation Problem

State estimation problems, also denoted as non-stationary inverse problems (Kaipio and Somersalo, 2004), use available measurements in conjunction with prior information about the physical phenomena and the measuring data in order to estimate the desired dynamic variables in sequence. This is performed in such a manner that the error is minimized statistically (Winkler, 2003).

In order to define the state estimation problem, two stochastic processes are used to infer dynamic systems: the first describes the evolution of the state variable over time and the other is related to the measurement.

Consider a model for the evolution of the vector x as

$$x_k = f_k\left(x_{k-1}, u_{k-1}, \nu_{k-1}\right) \tag{4.5}$$

where the subscript $k = 1, 2...$, indicate a time instant t_k in a dynamic problem. The vector $x \in R^{n_x}$ is called the state vector and represents the quantities of interest to be dynamically estimated. This vector proceeds in agreement with the state evolution model given by Equation 4.5, where f is a function of the state variable x, input variable $u \in R^{n_p}$, and the state noise vector $\nu \in R^{n_\nu}$. Consider that measurements $z \in R^{n_z}$ are also available at t_k, $k = 1, 2...,$. The measurements are associated with the state variables x through the function h in the form:

$$z_k = h_k\left(x_k, n_k\right) \tag{4.6}$$

where $n \in R^{n_n}$ is the measurement noise. Equation 4.6 is known as the observation (measurement) model. The state estimation problem objective is to obtain information about x_k based on the state evolution model, Equation 4.5, and on the measurements $z_{1:k}$ given by the observation model, Equation 4.6.

The following assumptions are made for the models 4.5 and 4.6 (Kaipio and Somersalo, 2004; Arulampalam et al., 2001):

1. The sequence x_k for $k = 1, 2...$, is a Markovian process, that is,

$$\pi\left(x_k \middle| x_0, x_1, ..., x_{k-1}\right) = \pi\left(x_k \middle| x_{k-1}\right) \tag{4.7}$$

2. The sequence z_k for $k = 1, 2...$, is a Markovian process with respect to the history of x_k, that is,

$$\pi\left(z_k \middle| x_0, x_1, ..., x_{k-1}\right) = \pi\left(z_k \middle| x_{k-1}\right) \tag{4.8}$$

3. The sequence x_k depends on the past observations only through it's own history, that is,

$$\pi\left(x_k \middle| x_{k-1}, z_{1:k-1}\right) = \pi\left(x_k \middle| x_{k-1}\right) \tag{4.9}$$

where $\pi\left(a \middle| b\right)$ denotes the conditional probability of a when b is given. If the conditions 4.7 - 4.9 are satisfied, the two stochastic processes represented by 4.6 and 4.5 are called the evolution-observation model.

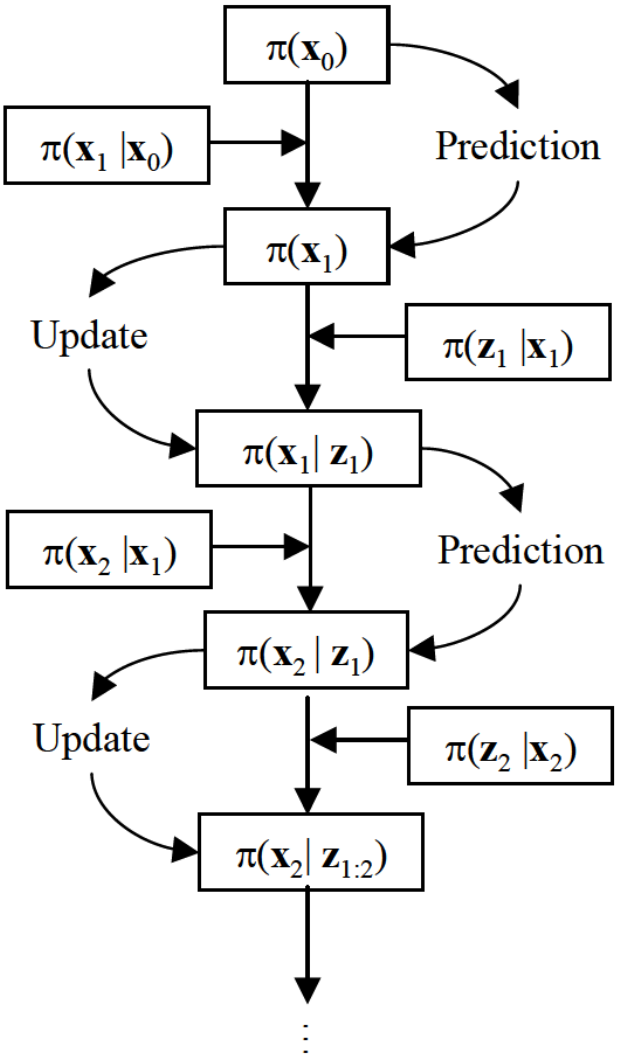

Figure 4.1: Prediction and update steps for the Bayesian filter (Kaipio and Somersalo, 2004).

For the state and observation noises, the following assumptions are made:

1. For $i \neq j$, the noise vectors v_i and v_j, as well as n_i and n_j, are mutually independent and also mutually independent of the initial state x_0.

2. The noise vectors v_i and n_j are mutually independent for all i and j.

The filtering problem for the evolution-observation model is when the objective is to obtain online information about $\pi\left(x_k|\, z_{1:k-1}\right)$. Assuming that $\pi\left(x_0|\, z_0\right) = \pi\left(x_0\right)$ is available, the posterior probability density $\pi\left(x_k|\, z_{1:k}\right)$is then obtained with Bayesian filters in two steps: prediction and update as shown in Figure 4.1.

4.1.3 Particle Filter

The sequential Monte Carlo technique, also known as the particle filter, is a recursive Bayesian filter based on Monte Carlo methods to simulate the distributions by random samples.

The idea of the method, of which the basis is the Sequential Importance Sampling (SIS) filter (Hammersley and Hanscomb, 1964), is to produce sequentially a group of random particles with associated weights to represent the required posterior density function and then compute estimates based on these samples and weights. As the number of these random particles increases and becomes sufficiently large, it becomes an equivalent representation to the usual functional description of the posterior PDF, approaching the optimal Bayesian estimate (Arulampalam et al., 2001).

In order to implement the main idea of the particle filter algorithm, let $\{x^i_{0:k}, i = 0, ..., N\}$ be the random particles with associated weights $\{w^i_k, i = 1, ..., N\}$ and let $x_{0:k} = \{x_j, j = 0, ..., k\}$ be the set of all states up to t_k, where N is the number of particles. The weights are normalized, so that $\sum_i w^i_k = 1$. Then, the posterior density at t_k can be discretely approximated by:

$$\pi\left(x_{0:k}|\, z_{1:k}\right) \approx \sum_{i=1}^{N} w^i_k \delta\left(x_{0:k} - x^i_{0:k}\right) \tag{4.10}$$

where δ is the Dirac delta function.

By taking hypotheses 4.7-4.9, the posterior density in Equation 4.10 can be written as

$$\pi\left(x_k|\, z_{1:k}\right) \approx \sum_{i}^{N} w^i_k \delta\left(x_k - x^i_k\right) \tag{4.11}$$

where the weights are chosen using the principle of importance sampling.

Utilizing the Bayes' theorem with recursive simulation, the weight update is written as

$$w^i_k \propto w^i_{k-1} \frac{\pi(z_k|x^i_k)\pi(x_k|x^i_{k-1})}{q(x_k|x^i_{k-1}, z_k)} \tag{4.12}$$

where $q(x_k|x^i_{k-1}, z_k)$ is the importance density. The most utilized choice consists in taking the importance density as the prior distribution, or

$$q(x_k|x^i_{k-1}, z_k) = \pi(x_k|x^i_{k-1}) \tag{4.13}$$

Figure 4.2 shows a sketch of the state estimation problem using the particle filter in the inverse problem.

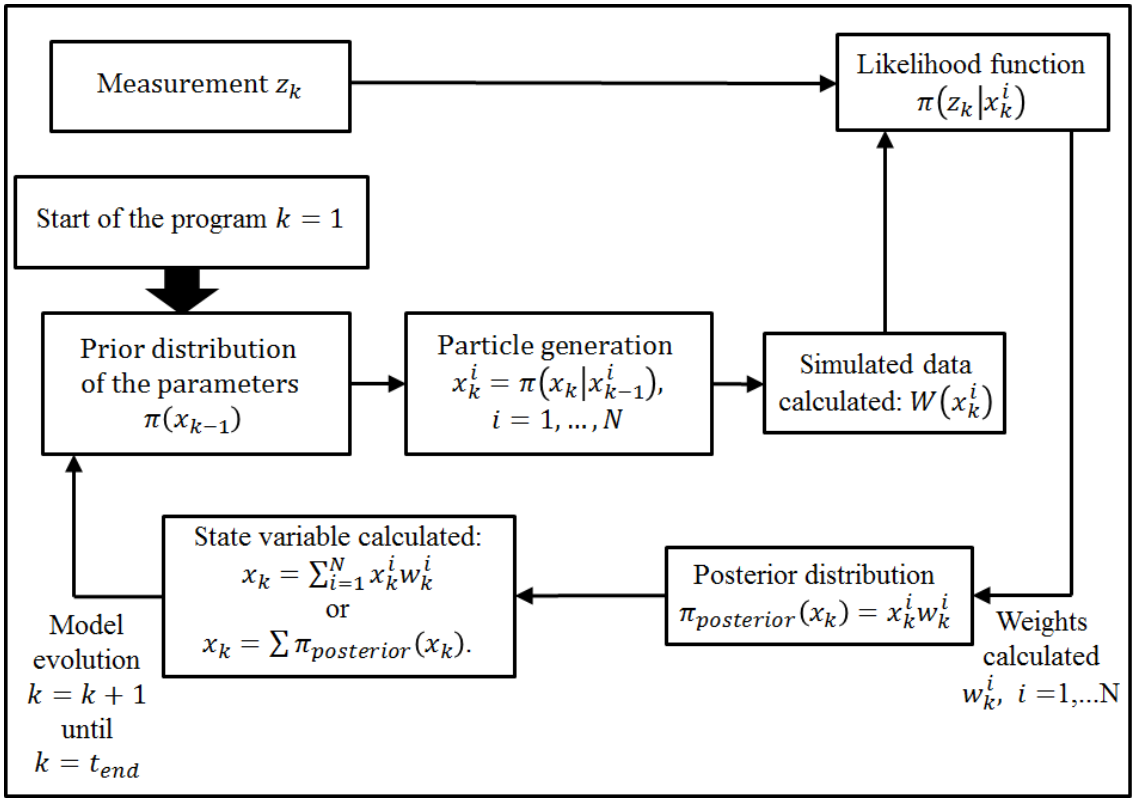

Figure 4.2: Sketch of the particle filter for the particle filter. (Silva, 2012)

The SIR filter

The SIR filter was first developed to overcome a common problem with the particle filter method, the degeneracy phenomenon (Gordon et al., 1993). It occurs when all but one particle may have negligible weight after a few iterations. This degeneracy implies that a higher computational effort is applied to constantly update particles in which their contribution is almost zero. To avoid the degeneracy problem, the resampling technique is used (Chen, 2003; Arulampalam et al., 2001). Resampling usually involves a mapping of the random measure $\{x_k^i, w_k^i\}$ into a random measure $\{x_k^{i*}, N^1\}$ with uniform weights. Figure 4.3 presents the process of particle selection through resampling.

Although the resampling step reduces the degeneracy problem, it may lead to a loss of particle diversity. This problem can be severe in the case of small evolution model noise. The steps of the SIR algorithm are detailed in Table 4.1.

Table 4.1: Algorithm of the SIR filter (Silva, 2012)

1.	Initialization
	1.1. Do $k = 1$
	1.2. Draw a group of particles with the initial distribution $x_k^i = \pi\left(x_k | x_{k-1}^i\right)$
2.	Weight Evaluation
	2.1. Evaluate the weights: $w_k^i = \pi\left(z_k | x_k^j\right)$
	2.2. Normalize the weights: $\hat{w}_k^i = \frac{w_k^i}{\sum_{i=1}^N w_k^i}$
3.	Resampling
	3.1. Construct the cumulative sum of weights (CSW) by computing $c_i = c_{i-1} + \hat{w}_k^i$ for $i = 1, ..., N$ with $c_0 = 0$
	3.2. Let $i = 1$ and draw a starting point ζ_1 from the uniform distribution $U[0, N^{-1}]$
	3.3. For $j = 1, ..., N$, do:
	3.3.1. Evaluate $\zeta_j = \zeta_1 + N^{-1}(j-1)$
	3.3.2. While $\zeta_j > c_i$ make $i = i + 1$
	3.3.3. Assign sample $x_k^j = x_k^i$
	3.3.4. Assign sample $w_k^j = N^{-1}$
4.	Posterior Mean Evaluation
	4.1. Evaluate the mean: $x_k = \sum_{i=1}^N x_k^i \cdot w_k^i$
5.	Model Evolution
	5.2. Do $x_k^i = \pi\left(x_k | x_{k-1}^i\right)$ for $i = 1, ..., N$
6.	Return to step 2

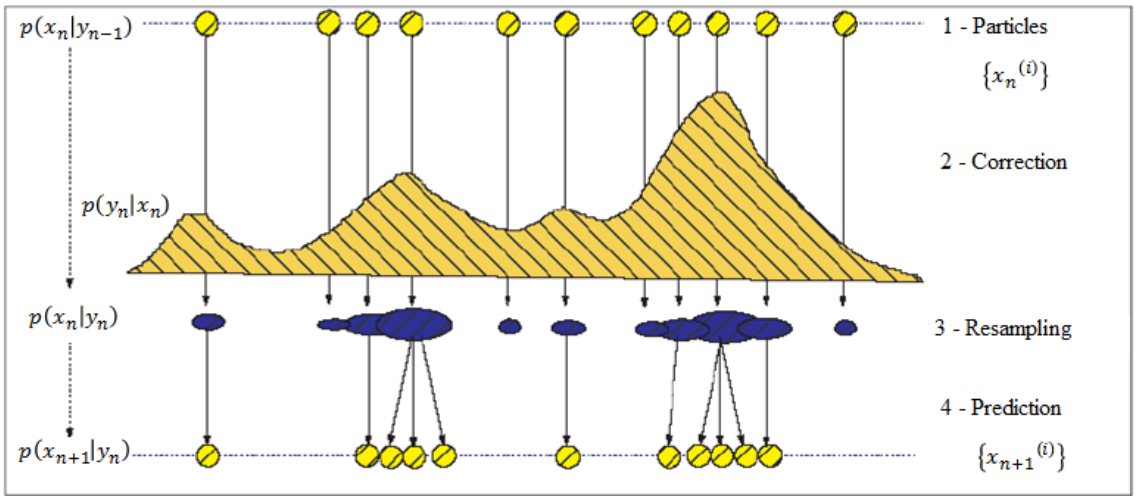

Figure 4.3: Resampling method (Chen, 2003)

The ASIR filter

The main idea of the ASIR algorithm filter is to increase the influence of the particles that have a better predictive probability (Pitt and Shephard, 1999). Less informative particles are discarded according to the regions of lesser importance, given by the probability function. The algorithm can be seen in Table 4.2.

According to Chen (2003), the advantage of the ASIR algorithm is that the ASIR filter avoids inefficient sampling because the particles to be sampled are directed to the high likelihood region, thus causing those particles to be more informative. However, if the process noise is large, the superiority of the ASIR filter is not guaranteed as a single point does not characterize $\pi(x_k|x_{k-1}^i)$ well, and the resampling of the ASIR filter is based on a poor approximation of $\pi(x_k|x_{k-1}^i)$ (Arulampalam et al., 2001).

Various algorithms for the implementation of different particle filters can be found in Doucet et al. (2001).

Table 4.2: Algorithm of the ASIR filter (Silva, 2012)

1.	Initialization
	1.1. Do $k = 1$
	1.2. Draw a group of new particles of the initial distribution $\pi(x_0)$ and obtain $\{(x_k^i, w_k^i); i = 1, ..., N\}$
2.	Samples of the Auxiliary Variable Evaluation
	2.1. Evaluate the samples: $u_k^i = E[x_k \vert x_{k-1}^i]$ or $u_k^i \approx \pi(x_k \vert x_{k-1}^i)$
3.	Auxiliary Variable Weight Evaluation
	3.1. Evaluate the likelihood function: $w_k^i = w_{k-1}^i \pi(z_k \vert u_k^i)$
	3.2. Normalize the weights:$\hat{w}_k^i = \frac{w_k^i}{\sum_k^N w_k^i}$
4.	Resampling
	4.1. Construct the cumulative sum of weights (CSW) by computing $c_i = c_{i-1} + \hat{w}_k^i$ for $i = 1, ..., N$ with $c_0 = 0$
	4.2. Let $i = 1$ and draw a starting point ζ_1 from the uniform distribution $U[0, N^{-1}]$
	4.3. For $j = 1, ..., N$, do:
	4.3.1. Evaluate $\zeta_j = \zeta_1 + N^{-1}(j-1)$
	4.3.2. While $\zeta_j > c_i$ make $i = i + 1$
	4.3.3. Assign sample $u_k^{\beta j} = u_k^i$
5.	Weight of the Selected Particles Evaluation
	5.1. Evaluate the weight of the selected particles: $\pi(z_k \vert u_k^{\beta j})$
6.	Samples Drawing
	6.1. Evaluate particles from the selected samples: $x_k^i = \pi(x_k \vert x_{k-1}^{ij})$ for $i = 1, ..., N$.
7.	Weight Evaluation
	7.1. Evaluate the likelihood function: $\pi(z_k \vert x_k^i)$
	7.2. Evaluate the new weights: $w_k^i = \frac{\pi(z_k \vert x_k^i)}{\pi(z_k \vert u_k^{\beta i})}$
	7.3. Normalize the weights: $\hat{w}_k^i = \frac{w_k^i}{\sum_k^N w_k^i}$
8.	Posterior Mean Evaluation
	8.1. Evaluate the mean: $x_k = \sum_{i=1}^N x_k^i \cdot \hat{w}_k^i$
9.	Model Evolution
	9.1. Do $k = k + 1$. If $k = k_{end} + 1$, stop.
10.	Return to step 2

4.2 Corrosion Model

It is accepted that corrosion of Fe may happen by an anodic reaction and a cathodic reaction (Postlethwaite et al., 1974, 1986; Slaimana and Hasan, 2010):

$$\begin{aligned} &2Fe \rightarrow 2Fe^{++} + 4e^{-} \\ &4H^{+} + 4e \longrightarrow 2H_2 \end{aligned} \tag{4.14}$$

In the presence of O_2, depolarization of the cathodic products takes place as

$$O_2 + 2H_2O + 4e \longrightarrow 4OH^{-} \tag{4.15}$$

However, Equation 4.15 is in general so rapid that the reaction is controlled by the diffusion of oxygen to the reacting surface. Also, the rate of O_2 depolarization depends on the rate of the diffusion of O_2 through the resistant films at the surface of the metal. One of the diffusion resistances is due to the precipitation of corrosion product

$$\begin{aligned} &Fe + H_2O + \frac{1}{4}O_2 \longrightarrow Fe\,(OH)_2 \\ &Fe\,(OH)_2 + \frac{1}{2}H_2O + \frac{1}{4}O_2 \longrightarrow Fe\,(OH)_3 \end{aligned} \tag{4.16}$$

Mahato et al. (1968a; 1968b) proposed a model based on two series resistances to diffusion. Dissolved O_2 in the flow must diffuse first through the fluid viscous sublayer, y_1, and then through a porous corrosion zone, y_2, to reach the material surface. Figure 4.4 presents the model described. The mass flux of O_2 n is

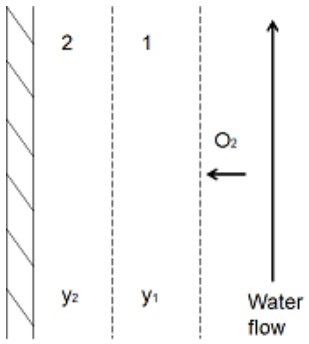

Figure 4.4: Sketch of the flow with mass transfer of oxygen to the surface causing the corrosion process.

$$\frac{dn}{dt} = \frac{(D_v + \epsilon)\,(C_b - C_i)}{y_1} \tag{4.17}$$

$$\frac{dn}{dt} = \frac{D_v\,(C_i - C_w)}{y_2} \tag{4.18}$$

where C_b is the bulk concentration of O_2, C_i is the concentration of O_2 at the interface of the solid wall and the turbulence boundary layer, and C_w is the concentration of O_2 at the surface of the base material.

The reaction in the pipe wall surface is so rapid that the concentration of O_2 in the wall is considered zero or negligibly small in comparison to the concentration of O_2 in the flow.

The mass transfer coefficient is

$$K_1 = \frac{(D_v + \epsilon)}{y_1} \tag{4.19}$$

$$K_2 = \frac{D_v}{y_2} \tag{4.20}$$

where D_v is the diffusivity of oxygen, and ϵ is the eddy diffusivity coefficient. The overall mass transfer coefficient is

$$\frac{1}{K_t} = \frac{1}{K_1} + \frac{1}{K_2} \tag{4.21}$$

The resistance offered by the corrosion product layer is given by Equation 4.22, assuming it to increase with the amount of corrosion and with a resistance coefficient k, which is independent of time.

$$y_2 = \int_0^t k \frac{dn}{dt} dt = kn \tag{4.22}$$

The mass flux of O_2 is then obtained:

$$\frac{dn}{dt} = \frac{C_b}{\left(\frac{kn}{D_v} + \frac{y_1}{D_v + \epsilon}\right)} \tag{4.23}$$

The amount of corrosion W in terms of α and β is

$$\frac{dW}{dt} = \frac{1}{2\alpha W + \beta} \tag{4.24}$$

$$\alpha = \frac{k}{2 D_v C_b} \tag{4.25}$$

$$\beta = \frac{y_1}{C_b \left(D_v + \epsilon\right)} \tag{4.26}$$

4.3 Results and Discussion

Due to the unknown nature of the resistance coefficient, defined in Equation 4.22, the particle filter is applied to estimate the corrosion rates.

The physical problem was solved by the Runge-Kutta method. Measurements performed by Lotz and Postlethwaite (1990) over the length of a 1.8:1:2 contraction-expansion in two different times of 25 and 48 h were used for comparison and estimation of the state variables. An error of 1% of the maximum value of the measures was used in the measurement errors matrix. The chosen state variables were the amount of mass loss, alpha, and beta. The evolution model defined for alpha, beta, and amount of mass loss is given in Equation 4.27

$$\alpha_k = \alpha_{k-1} + \sigma X_i \qquad \beta_k = \beta_{k-1} + \sigma X_i \qquad W_k = W_{k-1} + \sigma X_i \tag{4.27}$$

where X_i are random numbers with normal distribution, zero mean and unitary standard deviation. The standard deviation σ is 0.01, 0.5, and 0.3 when modeling the evolution in time for the amount of mass loss, alpha, and beta respectively.

Two different initial guesses were made. Initial Guess 1 is the same order of magnitude as that of Mahato et al. (1968b): values of 2.6 $\times$ 10^7 s m^4 kg^{-2} for alpha and 2.6 $\times$ 10^5 s m^2 kg^{-1} for beta.

In Initial Guess 2, beta was calculated using the ANSYS CFX CFD code, due to the fact that beta parameters depend only on the flow, according to Equation 4.26. The diameter used in the simulation was 21.1 mm in the contraction. The total length was 420 mm. The Reynolds number was 3.4 $\times$ 10^5 in the minor section and 1.7 $\times$ 10^5 in the other sections. A steady state and turbulent flow are assumed. The Schmidt number is 369 and the salt water saturated with oxygen has a concentration of 6.23 mg L^{-1} (Lewis, 2006). Table 4.3 indicates the initial guesses in all positions along the geometry.

In order to examine whether the state variables could be estimated, a sensitivity analysis was implemented. The results can be seen in Figure 4.5. It shows higher values for alpha. It is evident that beta cannot be estimated well due to the high difference of alpha values in comparison with beta.

The numbers of particles used to advance the mass loss, alpha and beta over time were 100, 1000 and 10000 for the SIR and ASIR filters. Figures 4.6 and Figure 4.7 show the mass loss over time in five different positions estimated with Initial Guesses 1 and 2, respectively. The first three

Table 4.3: Initial guess assisted by the ANSYS CFX code.

x (mm)	$\alpha \times 10^{-6}$	$\beta \times 10^{-3}$
6.8	25.92	10.13
26.5		11.68
43.5		40.93
55.5		3.12
67.4		1.22
80.2		1.36
92.2		1.74
104.9		2.01
117.7		2.26
132.3		2.58
160.4		3.35
231.2		5.20
244.0		5.63
260.2		6.06
271.3		6.23
278.2		9.22
291.0		3.06
303.8		1.84
318.3		1.43
327.6		1.65
340.4		1.60
354.9		1.59
366.0		1.48
382.3		1.51
401.9		1.54
419.8		1.54

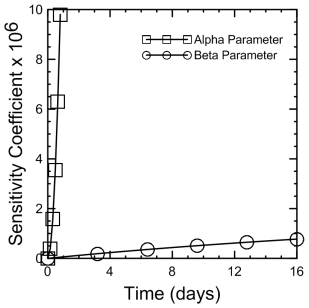

Figure 4.5: Sensitivity analysis for the parameters alpha and beta over time.

positions are upstream of the contraction at 6.8, 26.5, and 43.5 mm. The remaining positions are in regions with recirculation in the contraction at 55.5 mm and in the expansion at 318.3 mm.

It is noticed that increasing the number of particles further would not decrease the error of the estimated parameter. The ASIR filter shows a faster convergence with the experimental data. For the mass loss estimated with Initial Guess 2, it is observed that improving the initial guess increased the convergence with the experimental data. The differences observed in results with 100 particles between the SIR filter and the ASIR filter are due to the higher diversity that the new step in the ASIR filter produces to increase the number of particles with higher predictive probability.

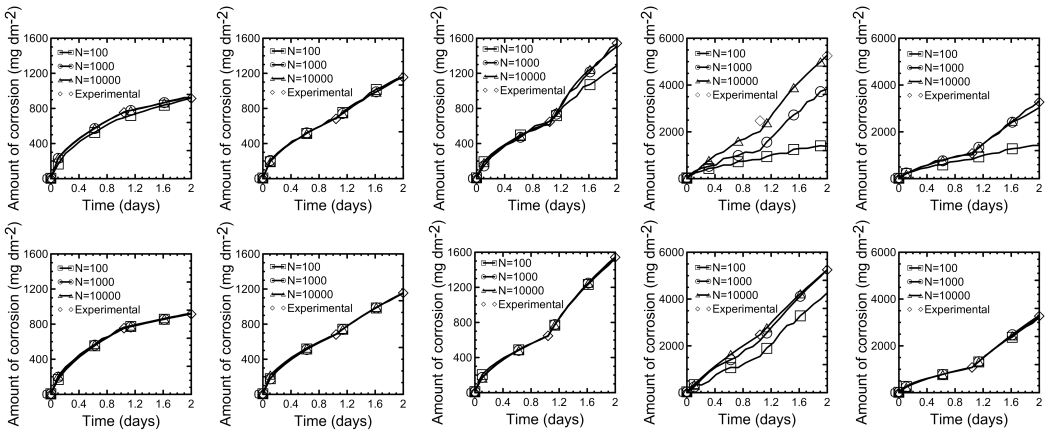

Figure 4.6: Estimated mass loss over time upstream of the contraction for different numbers of particles with Initial Guess 1 by the SIR and ASIR filters at 6.8, 26.5, 43.5, and 318.3 mm respectively.

The values of alpha and beta for both initial guesses estimated by the SIR and ASIR filters for 25 and 48 h are shown in Table 4.4 and 4.5 respectively. In all regions, there is a reduction of alpha over time estimated with the two initial guesses. The results for beta also show a reduction, but since the sensitivity of beta is small in the results, beta is considered constant in time. Comparing

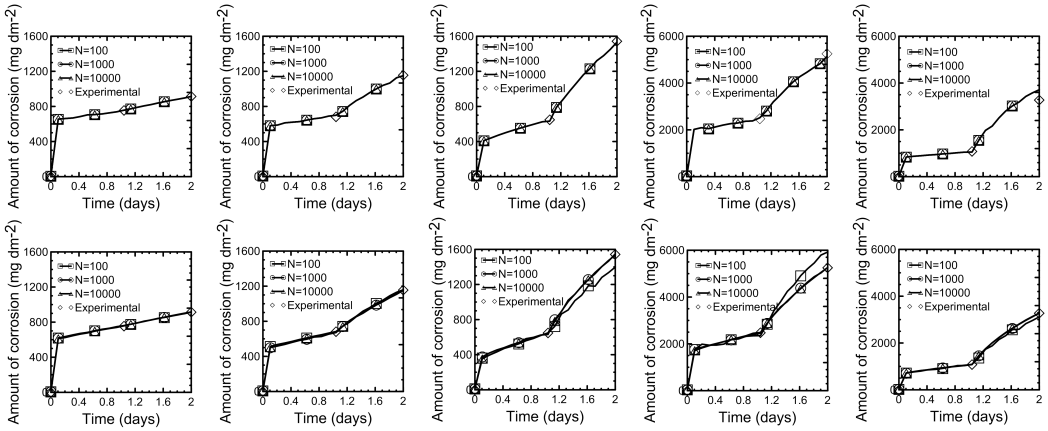

Figure 4.7: Estimated mass loss over time upstream of the contraction for different numbers of particles with Initial Guess 2 by the SIR and ASIR filters at 6.8, 26.5, 43.5, and 318.3 mm respectively.

the results estimated with Initial Guesses 1 and 2, an overall increase in alpha is observed in all regions. The contraction region has a lower value of alpha, in the region where the retention of the corrosion products is lower according to Lotz and Postlethwaite (1990), between 43.5 and 271 mm. This could be related to the sudden increase in turbulence levels due to the change of geometry. This disturbance caused a higher loss of corrosion products, increasing the mass loss rates.

Figures 4.8 and 4.9 show the amount of mass loss as a state variable in the length estimated for 25 and 48 h by the application of the SIR and ASIR filters with Initial Guesses 1 and 2 respectively. It is observed that the ASIR filter obtained a better estimation in the contraction region, between 55.5 and 271.3 mm, for 25 and 48 h. Disparities were higher for the time of 25 h. The results estimated with Initial Guess 2 showed a better accuracy.

In order to investigate whether the parameters alpha and beta were well estimated, the weight loss rate was calculated by Equation 4.24. Figure 4.10 presents the corrosion rate along the geometry in 25 and 48 h calculated using the parameters estimated with Initial Guess 1 with the SIR and ASIR filters with a 99% confidence interval.

A loss of particle diversity is observed in the contraction region with the estimation of the SIR filter. The results obtained by the ASIR filter presented a high variance. This can be explained by the fact that the state space of the Initial Guess 1 may not have been properly chosen. The ASIR filter, in that case, degraded the performance, increasing the number of bad particles compared with the SIR filter. Disparities were higher in the region upstream of the expansion, between

Table 4.4: Alpha and beta estimated with Initial Guess 1.

	SIR filter				ASIR filter			
	$\alpha \times 10^{-6}$		$\beta \times 10^{-3}$		$\alpha \times 10^{-6}$		$\beta \times 10^{-3}$	
x (mm)	25 h	48 h	25 h	48 h	25 h	48 h	25 h	48 h
6.8	11.31	20.52	178.17	167.83	9.83	22.97	202.03	198.51
26.5	12.82	6.35	220.38	231.76	13.65	6.72	159.95	162.88
43.5	14.55	2.91	221.25	105.09	13.78	2.65	245.97	154.96
55.5	0.40	0.17	266.49	79.72	0.34	0.12	211.78	149.54
67.4	0.40	0.04	266.49	142.28	0.07	0.09	162.31	275.20
80.2	0.40	0.06	266.49	76.97	0.12	0.06	170.16	102.75
92.2	0.40	0.03	266.49	63.25	0.07	0.02	181.82	130.57
104.9	0.40	0.04	266.49	113.45	0.28	0.09	131.89	93.15
117.7	0.40	0.10	266.49	59.59	0.06	0.05	229.90	118.44
132.3	0.40	0.20	266.49	7.20	0.13	0.17	169.55	69.79
160.4	0.40	0.02	266.49	126.85	0.28	0.10	226.66	80.65
231.2	0.40	0.11	266.49	78.55	0.06	0.05	234.02	194.35
244.0	0.40	0.04	266.49	141.49	0.07	0.08	181.23	180.53
260.2	0.40	0.04	266.49	142.28	0.07	0.09	181.08	222.85
271.3	16.26	22.75	226.55	254.88	14.64	0.12	268.79	87.09
278.2	3.01	1.95	221.75	228.17	3.38	2.16	186.75	180.92
291.0	13.17	1.28	214.54	169.09	13.38	1.25	178.06	176.39
303.8	3.03	1.55	221.15	155.22	2.88	1.27	237.64	232.48
318.3	3.84	0.07	248.09	268.62	3.89	0.15	250.68	239.14
327.6	2.78	0.60	178.55	113.64	2.37	0.48	180.59	177.26
340.4	3.48	0.31	176.87	135.75	2.97	0.20	231.94	183.39
354.9	2.53	0.37	223.09	85.11	2.72	0.36	124.47	114.81
366.0	1.11	0.47	279.12	159.76	1.59	0.32	243.50	219.64
382.3	1.55	0.37	275.67	171.70	2.33	0.53	138.31	95.25
401.9	8.18	0.32	201.57	245.61	7.35	0.32	224.53	179.96
419.8	2.44	0.93	52.59	56.73	1.23	0.52	219.88	243.34

Table 4.5: Alpha and beta estimated with Initial Guess 2.

	SIR filter				ASIR filter			
	$\alpha \times 10^{-6}$		$\beta \times 10^{-3}$		$\alpha \times 10^{-6}$		$\beta \times 10^{-3}$	
x (mm)	25 h	48 h	25 h	48 h	25 h	48 h	25 h	48 h
6.8	43.11	25.84	15.05	15.38	32.36	24.86	9.52	8.86
26.5	41.30	7.65	15.24	17.04	30.83	7.48	12.64	13.63
43.5	26.13	3.32	39.17	44.71	22.03	3.23	40.09	37.04
55.5	3.35	0.33	2.28	2.52	1.95	0.30	4.11	4.02
67.4	2.00	0.37	0.75	0.83	1.11	0.38	1.58	1.43
80.2	1.87	0.15	1.66	1.22	1.07	0.15	1.67	2.03
92.2	2.03	0.14	0.85	0.38	1.04	0.13	1.70	1.58
104.9	1.99	0.18	1.32	1.69	1.21	0.18	1.61	1.44
117.7	2.20	0.19	1.47	1.64	1.39	0.17	2.15	2.09
132.3	2.03	0.25	1.28	1.59	1.16	0.24	2.65	3.46
160.4	2.82	0.20	2.61	2.96	1.80	0.19	3.65	3.56
231.2	1.87	0.25	6.22	8.19	1.39	0.27	4.44	3.29
244.0	1.11	0.25	6.05	5.83	0.87	0.26	5.79	6.10
260.2	1.11	0.31	6.51	6.60	0.84	0.33	6.49	7.06
271.3	22.05	0.19	5.78	5.50	20.37	0.20	6.67	6.30
278.2	14.65	2.71	7.53	8.42	9.81	2.74	7.56	8.83
291.0	36.68	2.38	2.72	2.29	25.01	1.88	4.00	4.19
303.8	16.88	2.03	1.79	2.06	10.60	1.92	2.17	1.98
318.3	14.96	0.52	1.37	1.75	9.92	0.69	1.43	1.39
327.6	11.04	0.87	1.57	1.93	7.12	0.88	1.78	1.68
340.4	11.75	0.76	1.56	1.31	7.88	0.57	1.66	1.63
354.9	9.82	0.64	1.51	1.26	6.27	0.57	0.94	0.91
366.0	9.77	0.77	1.42	1.75	6.32	0.79	0.89	0.83
382.3	9.81	0.78	1.44	1.77	6.33	0.72	0.95	0.88
401.9	21.19	0.74	1.45	1.85	14.65	0.78	1.46	1.44
419.8	8.88	1.11	1.34	1.64	5.54	1.06	1.60	1.71

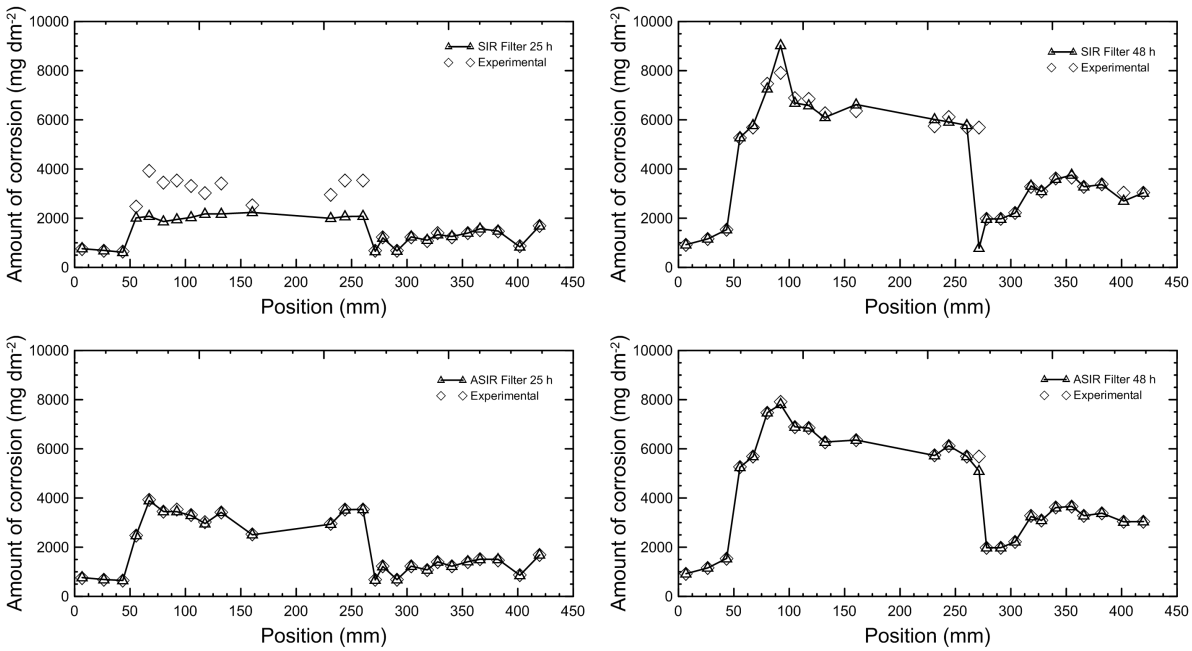

Figure 4.8: Estimated mass loss through the geometry with the SIR filter and the ASIR filter in 25 and 48 h with Initial Guess 1.

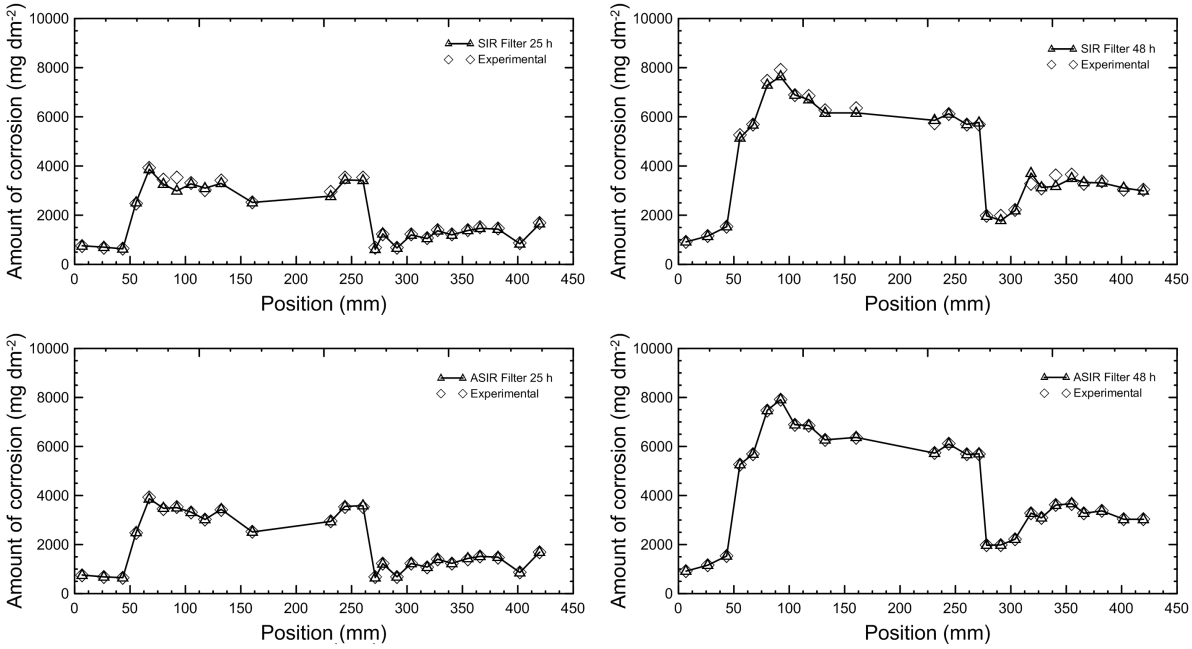

Figure 4.9: Estimated mass loss through the geometry with the SIR filter and the ASIR filter in 25 and 48 h with Initial Guess 2.

231.2 and 271.3 mm.

Figure 4.11 shows the corrosion rates calculated by alpha and beta estimated with Initial Guess 2. The results shows a better agreement with the experimental data. The proper selection of the initial guess improved the performance of the SIR and ASIR filters.

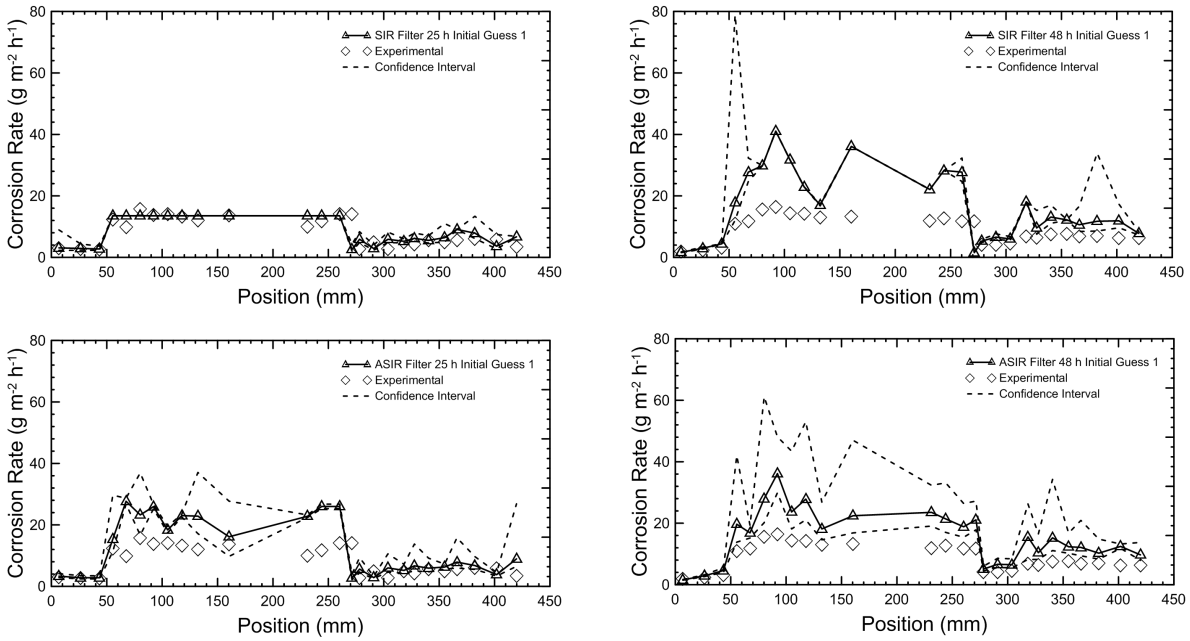

Figure 4.10: Mass loss rate through the geometry in 25 and 48 h calculated with alpha and beta estimated by SIR and ASIR filters using Initial Guess 1.

Lotz and Postlethwaite (1990) define the retention factor as the ratio between the products of corrosion and mass loss, or

$$R = \frac{Local\ mass\ of\ corrosion\ products}{Local\ metal\ mass\ loss} \tag{4.28}$$

It is shown in Figure 4.12 that the resistance coefficient of alpha, defined in Equation 4.22, is related to the retention of corrosion products as it displays the same behavior along the geometry. The evolution in time of alpha provides information about the morphology of the corrosion products. Nevertheless, the model does not account for the changes in time of the resistance coefficient that occur and that may affect the accuracy of the estimations.

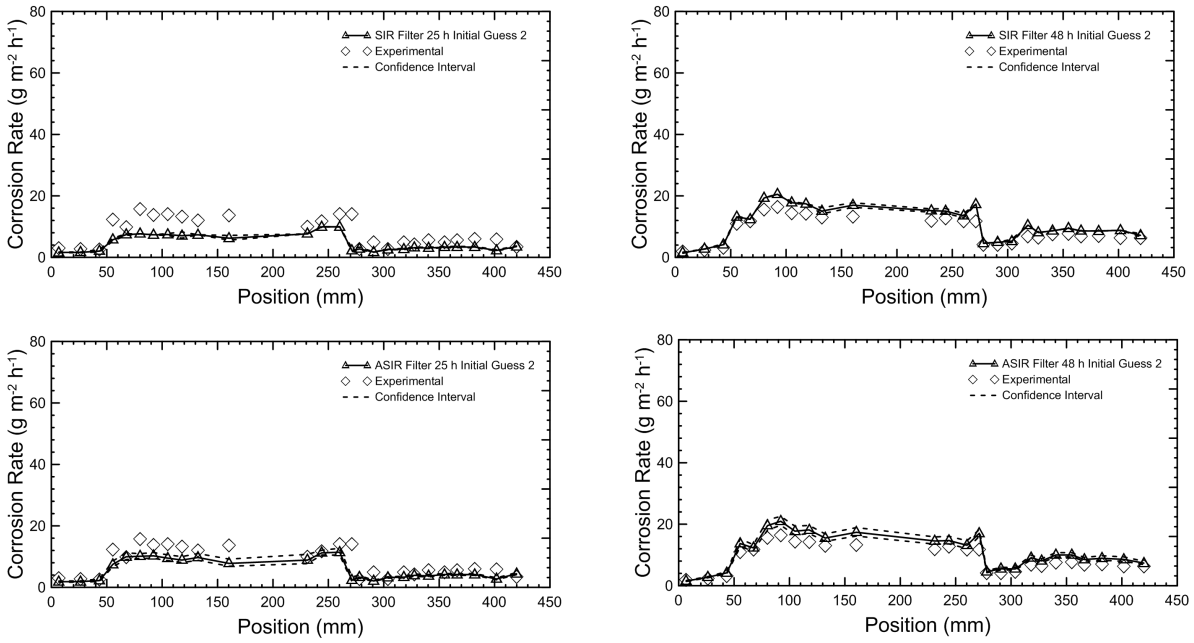

Figure 4.11: Mass loss rate through the geometry in 25 and 48 h calculated with alpha and beta estimated by SIR and ASIR filters using Initial Guess 2.

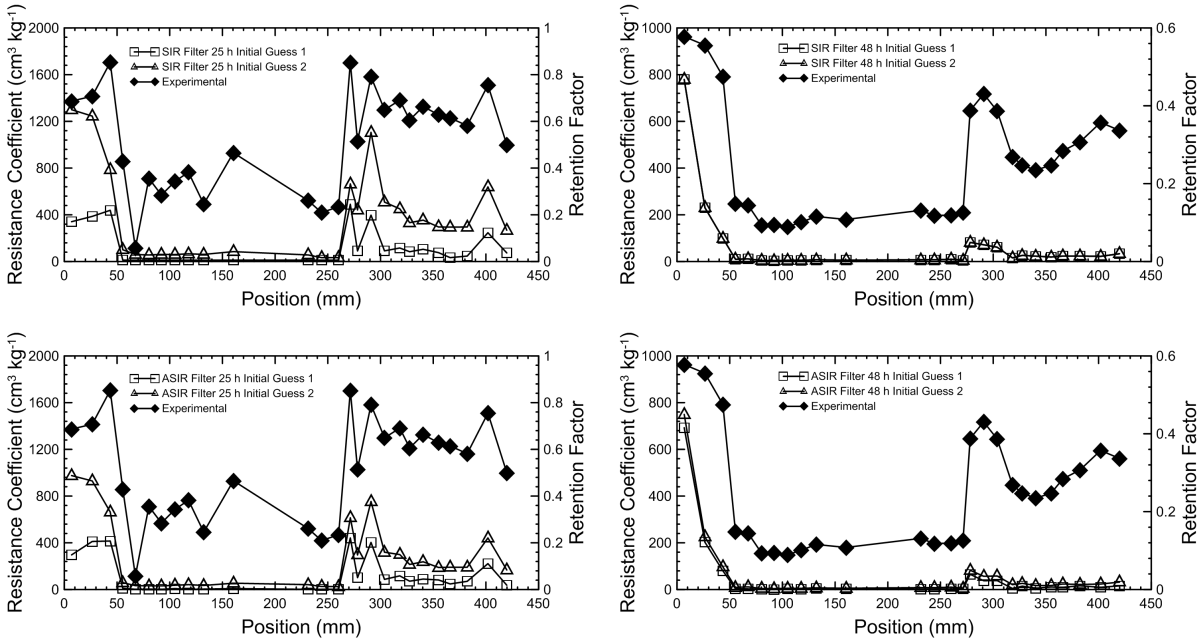

Figure 4.12: Retention factor compared to the resistance coefficient in 25 and 48 h.

Chapter 5

Comparison of Results and Discussion

The main objective of this work is to analyze the two models of corrosion adopted in this work. The main difference between those models is how the resistance to mass transfer is treated. In the first model, it is considered that oxygen diffuses through the boundary layer and reaches the wall, where it is consumed by the corrosion reaction. The second model considers that the oxygen firstly diffuses through an oxide resulting from the corrosion process, named the corrosion products. Two different methods are applied to investigate the models.

In Chapter 3, the mass transfer is computed by the use of CFD. The equations of mass, momentum, and species conservation are solved. Thus, the values of the mass transfer coefficient are evaluated by the definition expressed by Equation 3.21, considering the values of diffusion and concentration to be constant in the domain.

In Chapter 4, the mass transfer is estimated by the inverse problem due to the unknown nature of the resistance coefficient, defined in Equation 4.22. Experimental data from the literature are used to estimate the state variables of the model. Values of alpha related to the corrosion products expressed by Equation 4.25 and values of beta related to the flow expressed by Equation 4.26 are estimated by the SIR and ASIR filters.

The results are compared in Figures 5.1 and 5.2. It is observed that the results are improved by the resistance modeling of the corrosion products that precipitate in the base material. The mean errors of the SIR filter are 42.61% in 25 h and 22.21% in 48 h. Average ASIR filter errors are 29.86 and 25.36% in 25 h and 48 h respectively. CFD average errors are 175.81 and 136.83% in 25 and 48 h. The errors in each position are detailed in Table 5.1.

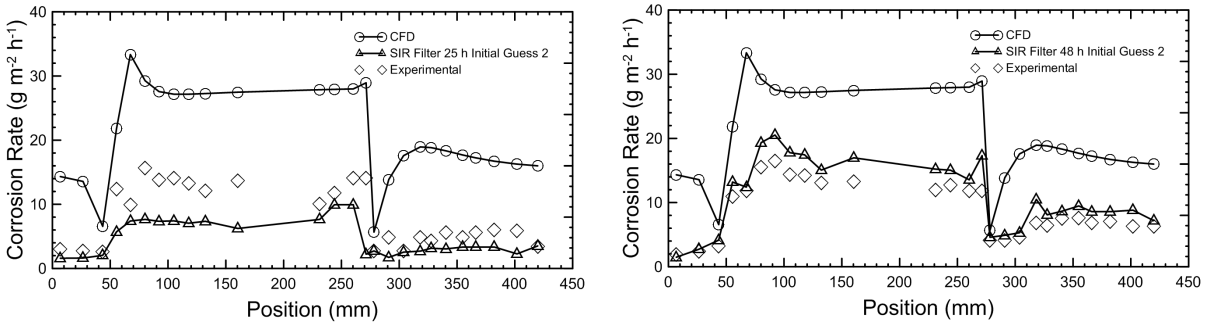

Figure 5.1: Mass loss rates through the geometry with CFD and SIR filter in 25 and 48 h.

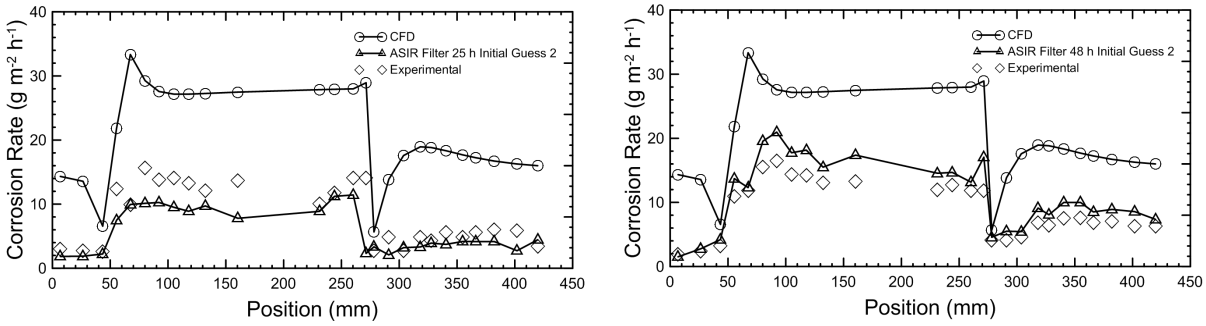

Figure 5.2: Mass loss rates through the geometry with CFD and ASIR filter in 25 and 48 h.

It is noticed that neglecting the corrosion products' resistance introduces considerable error into the model. However, modeling only the concentration boundary layer resistance by the application of CFD can still be useful for a qualitative analysis, as it shows the critical regions. The high computational effort of calculating large time intervals in CFD is also a drawback. The mass transfer coefficients are simplified to be time independent in the model solved by CFD.

Another advantage of the inverse problem approach is the possibility of predicting mass loss despite the few measurements of mass loss over time. It is a complicated task to obtain a large number of experimental measurements due to the kinetics that causes the corrosion reaction to happen over an extended time interval, taking days and even months to occur. Figure 5.3 shows the corrosion rates' curves obtained by the estimation of alpha and beta upstream of the contraction in 6.8, 26.5, and 43.5 mm and in the recirculation regions in 55.5 and 318.3 mm. The results were well estimated, although there were only three experimental points over time. The dislocation of the curves occurred due to the influence of time on the resistance coefficient.

In the case of mass loss treated as a state variable, the errors are lower. The estimation errors of the SIR filter are 2.51% in 25 h and 1.75% in 48 h. ASIR filter errors are 0.36 and 0.11% in 25 and 48 h respectively. Details of the errors estimated for the amount of corrosion are displayed in Table 5.2.

Table 5.1: Error of mass loss rate calculated by mass transfer with CFD, and with the inverse problem in 25 and 48 h.

	SIR filter		ASIR filter		CFD	
x (mm)	25 h (%)	48 h (%)	25 h (%)	48 h (%)	25 h (%)	48 h (%)
6.8	47.30	22.16	39.17	20.64	373.56	650.41
26.5	40.48	13.27	31.12	14.57	395.58	462.50
43.5	21.02	28.96	14.00	30.74	153.10	104.12
55.5	53.82	20.47	39.56	25.19	76.09	99.19
67.4	25.55	4.65	0.12	3.79	235.39	181.17
80.2	51.29	24.17	35.50	25.53	86.30	87.84
92.2	46.85	24.54	25.80	27.20	99.34	67.29
104.9	47.44	23.71	32.60	23.47	92.41	89.05
117.7	46.80	22.27	32.94	27.23	104.90	90.33
132.3	39.25	15.31	19.67	18.65	125.25	108.67
160.4	54.42	27.95	43.05	30.96	100.74	107.14
231.2	24.15	27.16	11.90	21.66	176.23	132.96
244.0	15.85	17.89	5.02	15.02	136.26	118.71
260.2	29.59	14.21	19.01	10.94	98.20	136.00
271.3	84.21	45.99	83.57	43.78	104.92	144.00
278.2	0.06	11.33	22.08	10.87	107.11	37.61
291.0	64.71	18.92	57.26	33.59	183.13	236.62
303.8	6.91	14.63	17.46	17.85	542.42	280.44
318.3	44.74	53.46	32.15	33.41	286.72	177.22
327.6	27.10	25.78	9.25	25.54	335.78	192.87
340.4	45.64	14.87	33.64	32.51	226.25	143.23
354.9	31.79	24.00	14.65	30.89	261.08	131.60
366.0	40.40	25.81	25.91	24.65	206.93	152.39
382.3	44.75	22.00	31.21	26.60	176.29	137.67
401.9	61.50	39.17	53.70	35.19	175.38	156.94
419.8	1.62	13.48	28.59	16.17	362.66	152.69

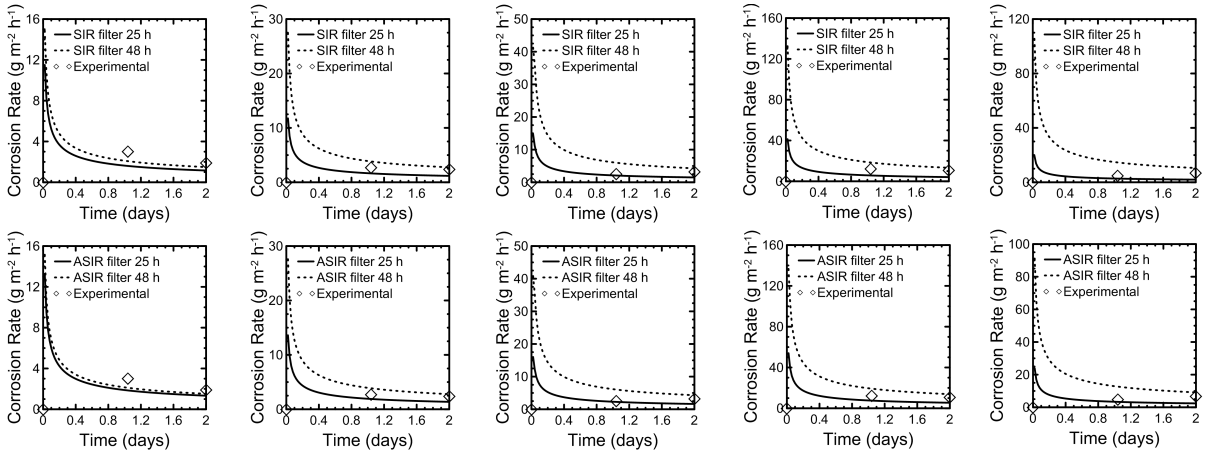

Figure 5.3: Mass loss rates' curves obtained by the SIR and ASIR filters in 6.8, 26.5, 43.5, 55.5, and 318.3 mm respectively.

In the region between 6.8 and 43.5 mm, where the flow is assumed to be developed, the predictions have a good performance, with errors lower than 3%. The complex hydrodynamic pattern in the contraction and expansion could be related to the increasing errors. In those regions, where recirculation occurs, errors tend to be higher.

Table 5.2: Error in amount of corrosion estimated with SIR and ASIR filters for 25 and 48 h.

	SIR filter		ASIR filter	
x (mm)	25 hours (%)	48 hours (%)	25 hours (%)	48 hours (%)
6.8	0.08	0.27	0.16	0.04
26.5	2.15	0.63	0.50	0.00
43.5	2.50	0.75	0.07	0.61
55.5	18.73	2.18	19.72	0.08
67.4	55.59	0.25	55.73	0.11
80.2	16.99	2.46	11.39	0.02
92.2	13.68	3.48	1.36	0.01
104.9	7.28	0.06	5.82	0.13
117.7	6.43	2.26	8.74	0.11
132.3	8.84	1.82	13.57	0.01
160.4	26.42	3.23	12.57	0.03
231.2	10.11	2.02	16.74	0.21
244.0	16.34	0.05	20.52	0.46
260.2	3.36	0.04	1.51	0.29
271.3	82.63	1.35	81.44	0.17
278.2	81.08	0.26	78.30	0.19
291.0	45.53	9.41	44.06	0.36
303.8	74.92	1.52	79.26	0.04
318.3	14.23	13.19	11.68	0.04
327.6	26.42	1.35	29.88	0.00
340.4	14.51	12.27	12.26	0.28
354.9	12.44	4.62	17.05	0.07
366.0	4.23	1.56	8.02	0.12
382.3	5.34	1.86	1.89	0.09
401.9	43.29	2.27	41.73	0.26
419.8	91.01	1.67	95.91	0.24

Chapter 6

Conclusion

In the present work, two different models of flow-accelerated corrosion were applied to investigate mass transfer by two approaches. Firstly, the equations of mass, momentum, and species were solved by the use of Computational Fluid Dynamics to compute the mass transfer coefficient. The corrosion model chosen does not account for the corrosion products as a resistance. The other method involves the application of Bayesian filters to a flow-accelerated corrosion problem to estimate the state variables related to the mass transfer coefficient. Those state variables are related to the flow and the corrosion products.

The values of mass loss rate are overestimated in all regions using CFD. The mean errors obtained by that approach are 175.81 and 136.83% in 25 and 48 h. The precipitation of corrosion products that occurs in the surface of the material works as a resistance to mass transfer of oxygen to the metal surface, decreasing the dissolution of the base material. This fact is not considered in the model, explaining the disparities that occur in the model.

The Sampling Importance Resampling (SIR) and Auxiliary Sampling Importance Resampling (ASIR) filters were applied with different number of particles to calculate the mass transfer coefficient and hence the mass loss rates. Both filters obtained good results when estimating the state variables, and the modeling of the corrosion products shows improvement. The mean errors when calculating the mass transfer by the state variables estimated by the SIR filter were 42.61 and 22.21% in 25 and 48 h respectively. When carrying out the estimation with the assistance of the ASIR filter, the errors were 28.86 and 25.36% in 25 and 48 h respectively. It was observed that the limitations of the model influenced the results, since the alpha parameter may change with time. The errors are reduced when they are directly estimated. The errors in the amount of

mass loss estimated with the SIR filter were 2.51 and 1.75% and those obtained with the ASIR filter were 0.36 and 0.11% in 25 and 48 h respectively.

Possibilities for future works include:

- investigating the influence of different evolution models and deviations of alpha and beta, as the values were chosen based on experience;
- investigating the influence of time on the resistance coefficient, related to the corrosion products, as it became clear that it has a major role in the parameter and could improve the model;
- investigating the application of particle filters in an erosion-corrosion problem to extend the validation of the method.

Bibliography

ANSYS-Inc. (2009). *ANSYS CFX-Pre User's Guide*. ANSYS Inc.

Arulampalam, S., Maskell, S., Gordon, N., and Clapp, T. (2001). A tutorial on particle filters for on-line non-linear/non-gaussian bayesian tracking. *IEEE Transactions on Signal Processing*, 50:174–188.

Berger, F. and Hau, K. (1977). Mass-transfer in turbulent pipe-flow measured by electrochemical method. *International Journal of Heat and Mass Transfer*, 20(11):1185–1194.

Chen, Z. (2003). Bayesian filtering: from Kalman filters to particle filters, and beyond. Technical report, McMaster University.

Colaço, M., Orlande, H., Silva, W., and Dulikravich, G. (2012). Application of a bayesian filter to estimate unknown heat fluxes in a natural convection problem. *Journal of Heat Transfer*, 134(9):10.

Davis, C. and Frawley, P. (2008). Modelling of erosion-corrosion in practical geometries. *Corrosion Science*, 51:769–775.

Doucet, A., Freitas, N., and Gordon, N. (2001). *Sequential Monte Carlo Methods in Practice*. New York: Springer.

Ferng, Y. M. and Lin, B. H. (2010). Predicting the wall thinning engendered by erosion-corrosion using cfd methodology. *Nuclear Engineering and Design*, 240:2836 – 2841.

Ferng, Y. M., Tseng, Y. S., Pei, B. S., and Wang, S. L. (2008). A two-phase methodology to predict fac wear sites in the piping system of a bwr. *Nuclear Engineering and Design*, 238:2189 – 2196.

Gordon, N. J., Salmond, D. J., and Smith, A. F. M. (1993). Novel approach to non-linear/non-gaussian bayesian state estimation. *Journal of the American Statistical Association.*, 94(446):590-599.

Hamilton, F., Colaço, M., Carvalho, R., and Leiroz, A. (2013). Heat transfer coefficient estimation of an internal combustion engine using particle filters. *Inverse Problems in Science and Engineering*, 22:483–506.

Hammersley, J. M. and Hanscomb, D. C. (1964). London: Chapman Hall.

Kaipio, J. and Somersalo, E. (2004). *Statistical and Computational Inverse Problems*, volume 160. Springer-Verlag.

Kalman, R. E. (1960). A new approach to linear filtering and prediction problems. *ASME Journal of Basic Engineering*, 82:35–45.

Keating, A. and Nesic, S. (1999). Numerical prediction of erosion-corrosion in bends. In *Second International Conference on CFD in the Minerals and Process Industries*, pages 229–236, Melbourne.

Launder, B. and Spalding, D. (1972). Lectures in mathematical models of turbulence. *London, New York: Academic Press*, 7:169.

Lewis, M. (2006). Dissolved oxygen. Technical report, U.S. Geological Survey.

Lin, C. H. and Ferng, Y. M. (2014). Predictions of hydrodynamic characteristics and corrosion rates using cfd in the piping systems of pressurized-water reactor power plant. *Annals of Nuclear Energy*, 65:214 – 222.

Lotz, U. and Postlethwaite, J. (1990). Erosion corrosion in disturbed 2 phase liquid particle flow. *Corrosion Science*, 30:95–106.

Mahato, B. K., Voora, S. K., and Shemilt, L. W. (1968a). Steel pipe corrosion under flow conditions-i. an isothermal correlation for a mass transfer model. *Corrosion Science*, 8:173–193.

Mahato, B. K., Voora, S. K., and Shemilt, L. W. (1968b). Steel pipe corrosion under flow conditions-ii. mass transfer correlation with temperature effects. *Corrosion Science*, 8:737–749.

Menter, F. (1994). 2-equation eddy-viscosity turbulence models for engineering applications. *AIAA Journal*, 32(8):1598–1605.

Nesic, S. (2006). Using computational fluid dynamics in combating erosion-corrosion. *Chemical Engineering Science*, 61:4086 – 4097.

Nesic, S., Adamopoulos, G., Postlethwaite, J., and Bergstrom, D. J. (1993). Modelling of turbulent flow and mass transfer with wall function and low-reynolds number closures. *Canadian Journal of Chemical Engineering*, 71:28–34.

Nesic, S. and Postlethwaite, J. (1991a). Hydrodynamics of disturbed flow and erosion corrosion.1. single-phase flow study. *Canadian Journal of Chemical Engineering*, 69:698–703.

Nesic, S. and Postlethwaite, J. (1991b). Hydrodynamics of disturbed flow and erosion corrosion.2. 2-phase flow study. *Canadian Journal of Chemical Engineering*, 69:704–710.

Nesic, S., Postlethwaite, J., and Bergstrom, D. (1992). Calculation of wall mass-transfer rates in separated aqueous flow using a low reynolds-number k-epsilon model. *International Journal of Heat and Mass Transfer*, 35(8):1977–1985.

Ozisik, N. and Orlande, H. (2000). *Inverse Heat Transfer: Fundamentals and Applications*. Taylor and Francis.

Patankar, S. (1980). *Numerical heat transfer and fluid flow. Series in computational methods in mechanics and thermal sciences*. McGraw-Hill.

Pitt, M. and Shephard, N. (1999). Filtering via simulation: Auxiliary particle filters. *Journal of the American Statistical Association.*, 94(446):590–599.

Postlethwaite, J., Dobbin, M. H., and Bergevin, K. (1986.). The role of oxygen mass-transfer in the erosion-corrosion of slurry pipelines. *Corrosion*, 42(9):514–521.

Postlethwaite, J., Tinker, E. B., and Hawrylak, M. W. (1974.). Erosion-corrosion in slurry pipelines. *Corrosion*, 30(8):285–290.

Poulson, B. (1993). Advances in understanding hydrodynamic effects on corrosion. *Corrosion Science*, 35:655 – 665.

Poulson, B. (1999). Complexities in predicting erosion corrosion. *Wear*, 233-235:497–504.

Roberge, P. R. (2004). *Corrosion testing made easy: erosion-corrosion*. NACE Press Book.

Silva, W. B. (2012). *Aplicação de filtros de partículas para a assimilação de dados em problemas de fronteira móvel*. PhD thesis, Universidade Federal do Rio de Janeiro.

Slaimana, Q. J. M. and Hasan, B. O. (2010). Study on corrosion rate of carbon steel pipe under turbulent flow conditions. *The Canadian Journal of Chemical Engineering*, 88:1114–1120.

Versteeg, H. and Malalasekera, W. (2007). *An introduction to computational fluid dynamics : the finite volume method*, volume 2nd ed. Pearson Education Ltd.

Wang, Y. and Postlethwaite, J. (1997). The application of low reynolds number k-epsilon turbulence model to corrosion modelling in the mass transfer entrance region. *Corrosion Science*, 39(7):1265–1283.

White, F. M. (1991). *Viscous fluid flow*, volume 2. New York: McGraw-Hill.

Wilcox, D. (1988). Re-assessment of the scale-determining equation for advanced turbulence models. *AIAA Journal*, 26:1299–1310.

Winkler, R. (2003). *An Introduction to Bayesian Inference and Decision*. Gainsville: Probabilistic Publishing.

Xiong, J., Koshizuka, S., and Sakai, M. (2011). Turbulence modeling for mass transfer enhancement by separation and reattachment with two-equation eddy-viscosity models. *Nuclear Engineering and Design*, 241(8):3190–3200.